



## Article

# Dynamic Characteristics of Vegetation Change Based on Reconstructed Heterogenous NDVI in Seismic Regions

Shaolin Wu <sup>1,2</sup>, Baofeng Di <sup>3,\*</sup>, Susan L. Ustin <sup>4</sup>, Man Sing Wong <sup>2,5</sup>, Basanta Raj Adhikari <sup>3,6</sup>, Ruixin Zhang <sup>1</sup> and Maoting Luo <sup>1</sup>

<sup>1</sup> College of Architecture and Environment, Sichuan University, Chengdu 610065, China

<sup>2</sup> Department of Land Surveying and Geo-Informatics, The Hong Kong Polytechnic University, Hong Kong SAR, China

<sup>3</sup> Institute for Disaster Management and Reconstruction, Sichuan University-The Hong Kong Polytechnic University, Chengdu 610207, China

<sup>4</sup> Institute of the Environment, University of California Davis, Davis, CA 95616, USA

<sup>5</sup> Research Institute for Land and Space, The Hong Kong Polytechnic University, Hong Kong SAR, China

<sup>6</sup> Department of Civil Engineering, Pulchowk Campus, Tribhuvan University, Lalitpur 44600, Nepal

\* Correspondence: dibaofeng@scu.edu.cn

**Abstract:** The need to protect forests and enhance the capacity of mountain ecosystems is highlighted in the U.N.'s Sustainable Development Goal (SDG) 15. The worst-hit areas of the 2008 Wenchuan Earthquake in southwest China were mountainous regions with high biodiversity and the impacted area is typical of other montane regions, with the need for detecting vegetation changes following the impacts of catastrophes. While the widely used remotely sensed vegetation indicator NDVI is available from various satellite data sources, these satellites are available for different monitoring periods and durations. Combining these datasets proved challenging to make a continuous characterization of vegetation change over an extended time period. In this study, compared with linear regression, multiple linear regression, and random forest, Convolutional Neural Networks (CNNs) performed best with an average  $R^2$  of 0.819 (leave-one-out cross-validation). Thus, the CNNs model was selected to establish the map of the overlapping periods of two remote-sensing products: SPOT-VGT NDVI and PROBA-V NDVI, to reconstruct a SPOT-VGT NDVI for the period from June 2014 to December 2018 in the worst-hit areas of the Wenchuan earthquake. We analyzed the original and reconstructed SPOT-VGT NDVI in the hard-hit areas of the Wenchuan earthquake from 1999 to 2018, and we concluded that NDVI showed an overall upward trend throughout the study period, but experienced a sharp decline in 2008 and reached its lowest value a year later (2009). Vegetation recovery was rapid from 2009 until 2011 after which, it returned to a pattern of slower natural growth (2012–2018). The Longmenshan fault zone experienced the greatest vegetation damage and initiation of recovery there has caused the overall regional average recovery to lag by 1–2 years. In areas where the land was denuded of vegetation (i.e., effectively all vegetation was stripped from the surface) after the earthquake, the damage exceeded what was experienced anywhere else in the entire study area, and by 2018 it remained unrestored. In the 15 years since the earthquake, the areas that were denuded were expected to recover to the level of restoration equivalent with the NDVI of 2007, as was the case in other earthquake-damaged regions. In addition to the earthquake and the immediate loss of vegetation, the Chinese government's Grain for Green Policy, the elevation ranges within the region, the forest's phenological conditions, and human activities all had an impact on vegetation recovery and restoration. The reconstructed NDVI provides a long-term continuous record, which contributes to the identifying changes that are improving predictive forest recovery models and to better vegetation management following catastrophic disturbances, such as earthquakes.

**Keywords:** NDVI reconstruction; Wenchuan earthquake; vegetation recovery; landslides



**Citation:** Wu, S.; Di, B.; Ustin, S.L.; Wong, M.S.; Adhikari, B.R.; Zhang, R.; Luo, M. Dynamic Characteristics of Vegetation Change Based on Reconstructed Heterogenous NDVI in Seismic Regions. *Remote Sens.* **2023**, *15*, 299. <https://doi.org/10.3390/rs15020299>

Academic Editor: Wenquan Zhu

Received: 8 November 2022

Revised: 22 December 2022

Accepted: 30 December 2022

Published: 4 January 2023



**Copyright:** © 2023 by the authors. Licensee MDPI, Basel, Switzerland. This article is an open access article distributed under the terms and conditions of the Creative Commons Attribution (CC BY) license (<https://creativecommons.org/licenses/by/4.0/>).

## 1. Introduction

The United Nations Sustainable Development Goals (SDGs) (<https://UNSTAT.SUN.ORG/SDGS/REPORT/2022>, accessed on 12 May 2022) call for joint world efforts to protect the Earth, end poverty, and ensure peace and prosperity for the world's people. SDG 15 proposed "Protect, restore and promote sustainable use of terrestrial ecosystems, sustainably manage forests . . . and halt and reverse land degradation and halt biodiversity loss". Mountain ecosystems are required to be protected by 2030 in order to strengthen the capacity of mountain ecosystems. However, the health of montane forest ecosystems is not only affected by climatic conditions, but they are also sensitive to external disturbances, especially catastrophes [1]. Disturbance and stresses that cause vegetation changes exceeding normal annual or interannual changes and successional patterns creates challenges for sustainable forest management. With less than 10 years to achieve SDGs, there is an urgent need to develop long-term indicators that can be used to monitor and evaluate changes in vegetation conditions caused by different driving forces from weather and climate conditions to disasters [2,3].

The catastrophic Wenchuan earthquake with a magnitude of MS 8.0 occurred in the Longmenshan Mountain Range, Sichuan, China on 12 May 2008. It extended 240 km along the Yingxiu-Beichuan fault and 72 km along the Guanxian-Jiangyou fault [4]. The earthquake caused devastating damage to the region, with at least 87,000 people dead or missing and about US\$ 130 billion in economic loss [5]. The initial earthquake destroyed extensive forest (919.9 km<sup>2</sup>) and shrub (338.6 km<sup>2</sup>) ecosystems [6], mainly impacting the mountainous upper reaches of the Yangtze River, an area identified as essential for ecological preservation in China [7,8]. The earthquake created ecological and physiographic imbalances that have led to numerous further natural disasters like landslides, debris flows, and debris flows that are activated by intense summer monsoon rains (May–September). The 200,000 mass wasting geohazards [9] that have occurred since then have destroyed large swaths of forest vegetation [10,11] and created a cycle of repeated ecological and physiographic damage.

Vegetation indices, based on the spectral signature of plants, provide a quantitative and qualitative assessment of vegetation cover by combining the reflectance from spectral bands using both linear and non-linear methods [12,13]. One of the most widely applied vegetation indices, the Normalized Difference Vegetation Index (NDVI), calculated from the visible red and near-infrared bands, has performed better in many cases than other indices. NDVI is a measure of the "greenness" of the vegetation and is correlated with leaf area, leaf biomass [14–16], canopy cover [17–20], and chlorophyll content [21–23], and is strongly related to photosynthetic capacity [24–26], fluorescence [27,28], and Net Primary Productivity [29–32]. NDVI has been used to describe ecosystem status, condition, disturbance, and change [33–38]. NDVI can be retrieved from many satellite instruments, including the Satellite for Observation of Earth VEGETATION (SPOT-VGT), the Moderate Resolution Imaging Spectroradiometer (MODIS), the Landsat Thematic Mapper (TM), Sentinel 2 Multi-spectral Instrument (MSI), and the Project for On-Board Autonomy Vegetation (PROBA-V). The results were dissimilar comparing different NDVI products, and the NDVI products from the single sensor were often incomplete in measuring vegetation conditions [39–42]. For the worst-hit areas in Wenchuan Earthquake, most of the research on the impact of the earthquake on vegetation damage and restoration is based on MODIS NDVI [10,43–45]. However, the results based on MODIS NDVI did not show the lag and long-term nature of vegetation damage (recovered to the pre-earthquake level before 2010), which is different from that observed in the field. The SPOT-VGT NDVI data can be another important reference for the vegetation cover change in the worst-hit areas in Wenchuan Earthquake. Firstly, there was an accurate indication of SPOT-VGT NDVI on evergreen broad-leaved forest and coniferous forest [46] (consistent with the main vegetation coverage types in the study area). Secondly, it was reported that the responses of SPOT-VGT NDVI and MODIS NDVI to the surface vegetation in Southwest China where the study area is located failed the correlation test [47].

The available period of SPOT-VGT NDVI is from April 1998 to May 2014, which has limitations in the long-term indication of vegetation coverage recovery in the study area. SPOT-VGT NDVI data reconstruction can break through the shackles of a single NDVI data source in the study area and support a comparison of the vegetation changes in the past 10 years before and after the earthquake. According to the source of information during computing, the basic methods of remote-sensing image reconstruction were classified into two categories: single-source based and multiple-sources based. The single-source-based methods do not rely on other auxiliary information and fill in missing data based on the spatiotemporal characteristics of the dataset itself, including filter techniques [48,49], function fitting [50,51], and temporal deep learning [52]. Multiple-sources-based methods need to establish a mapping between the main data and auxiliary data, and use the advantages of auxiliary data sources in data integrity to fill in the lack of main data, which is part of spatio-temporal data fusion, including function-based [40,41,53,54], spectral-based [55], and learning-based [56,57]. Data reconstruction from multiple data sources tended to have better performance and can be the basement of data fusion [58]. Spatio-temporal fusion, multi-source fusion, and machine-learning have become the trend of NDVI reconstruction [59]. The remote-sensing data reconstruction methods based on deep learning have also been successfully used by researchers because of its excellent performance and transferability [60,61]. Given that the PROBA-V sensor has similar spectral characteristics to SPOT-VGT with a small difference between the two in the blue, red, and near-infrared bands (RMSE = 0.003), PROBA-V NDVI was selected to assist in reconstructing long-sequence SPOT-VGT NDVI.

To sum up, in order to fully understand the vegetation changes in the disaster area in the 10 years before and after the earthquake, the SPOT-VGT NDVI data was selected for reconstruction and extension because of its superiority in the main vegetation representation and long-term sequence in the worst-hit areas in Wenchuan Earthquake. After the method comparison with linear regression, multiple linear regression, random forest, Convolutional Neural Networks (CNNs), and CNNs were selected to reconstruct the SPOT-VGT NDVI data after 2014 based on PROBA-V NDVI. Based on the 1998–2018 NDVI data composed of original data and reconstructed data, the spatiotemporal change patterns of vegetation in the worst-hit areas and the impact of earthquake were analyzed. This study provided a framework for comparison and reconstruction of multi-source (sensor) data, which improves the comprehensiveness and accuracy of long-term vegetation coverage understanding in the study area.

## 2. Data and Methods

### 2.1. Study Area

The worst-hit areas in Wenchuan Earthquake (Figure 1) cover about 119,056 km<sup>2</sup>, including 37 areas designated as worst-hit areas and 10 designated as most severely hit areas (The Assessment Report of Wenchuan Earthquake Disaster Scope). The worst-hit areas in Wenchuan Earthquake include a wide range of landforms, e.g., plains, hills, mountains, and plateaus. The southwest has the highest elevation, forming a narrow buffer zone against the low-elevation Chengdu Plain [62]. There are a large number of faults in the study area, so geological movement is active and geological disasters occur frequently.

The forests and other vegetation types vary across the region but generally include subtropical broadleaf evergreen forests (e.g., *Cinnamomum wilsonii*, *Quercus lanata*) that dominate up to about 1800 m, a mixed broadleaf (e.g., *Eucommia ulmoides*, *Quercus semecarpifolia*) and conifer forest from 1800 m to about 2200 m, and transition to conifer forests at higher elevations up to about 3300 m. Shrubs, e.g., *Rhododendron arboretum*) are common in the study area between 1800 and 3300 m [6]. High-elevation conifer forests are dominated by cold-tolerant *Abies* (true fir), *Picea* (Spruce), *Pinus* (Pine), and *Tsuga* (Hemlock) species. The eastern mountains have abundant *Abies*, *Picea*, and *Pinus* species. While semiarid shrublands dominate the west. Some areas only receive 600 mm annual precipitation and

are dominated by sparse alpine perennial vegetation like grasses, sedges, cushion plants, etc. Stone deserts are found at 5000 m and higher.

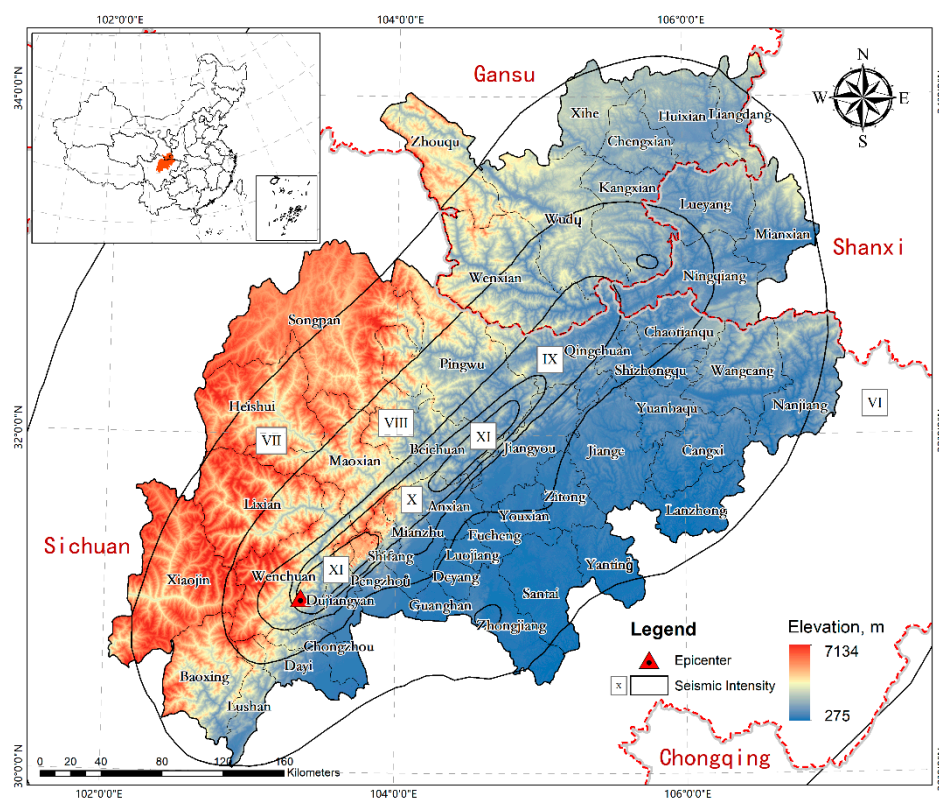


**Figure 1.** Study area: The worst-hit areas in the Wenchuan Earthquake.

## 2.2. Data Preparation

The SPOT-VGT NDVI and PROBA-V NDVI products were used as the source data. The two raw datasets are the composite product of 10-day MVC (Maximum Value Composite) with a spatial resolution of 1 km, which has been corrected by calibration and cloud monitoring [46,63–65]. PROBA-V NDVI was resampled to the position corresponding to SPOT-VGT NDVI image in the same geographic coordinate system (GCS\_WGS\_1984). Monthly data were synthesized by MVC to further reduce interference from varying solar elevation angles, clouds, aerosols, and other atmospheric factors [66]. In order to ensure sufficient data volume while avoiding model overfitting, the scale of the training data was set as the entire southwest region but excluding Xizang Province (1,339,647 pixels). The pixel value of PROBA-V NDVI is the feature variable, and the SPOT-VGT NDVI pixel value at the same time (2013.11–2014.05) and geographical location are the response variables. The size of  $43 \times 43$  pixels is a sample and there are 9,377,526 samples in the training dataset.

MODIS NDVI (MYD13A2 and MOD13A2) data were used to check the overall trend of reconstructed NDVI and compare between different sensors. The descriptions and sources of the main data are shown in Table 1.

## 2.3. Convolutional Neural Networks

Deep learning methods can be used to compute and obtain the characteristics found among nonlinear relationships through data operations, and these are used to achieve predictive models or classifications. Compared with general machine-learning methods, deep learning has a more complex structure, which makes its model performance superior in most cases [67]. As a representative of the class of deep-learning algorithms, convolutional neural networks (CNNs) have performed well in the processing and analysis of computer vision, based on its effective algorithms and structures [68]. The features extracted by filters in CNNs have been nonlinearly transformed by an activation function, which becomes

the input of the subsequent layer [68–70]. This results in the most valuable features in the image of the last layer being retained for prediction. In this study, linear regression, multiple linear regression, Random Forest, and CNNs were compared. The CNNs were found to have performed best on the training data set with  $R^2$  of 0.965 (Table S1). Therefore, CNNs were selected as the model for NDVI prediction.

**Table 1.** Description and source of data.

NDVI Dataset	Spatial Resolution	Time Range	Data Type	Data Source
Original SPOT-VGT	1 km	1998.04–2014.05	HDF4	<a href="https://www.vito-eodata.be/PDF/portal/Application.html#Home">https://www.vito-eodata.be/PDF/portal/Application.html#Home</a> (accessed on 12 May 2022)
PROBA-V	1 km	2013.11–2018.12	TIFF	<a href="https://www.vito-eodata.be/PDF/portal/Application.html#Home">https://www.vito-eodata.be/PDF/portal/Application.html#Home</a> (accessed on 12 May 2022)
MYD13A2	1 km	2003.01–2018.12	HDF	<a href="https://ladsweb.modaps.eosdis.nasa.gov/">https://ladsweb.modaps.eosdis.nasa.gov/</a> (accessed on 12 May 2022)
MOD13A3	1 km	2003.01–2018.12	HDF	<a href="https://ladsweb.modaps.eosdis.nasa.gov/">https://ladsweb.modaps.eosdis.nasa.gov/</a> (accessed on 12 May 2022)

To maximize the performance of the model within the available computational resources, the model architecture was defined by adjusting the types and numbers of networks through the pre-experiment using different model architectures (Figure 2). The proposed model consisted of four convolutional layers, four maximum pooling layers, eight batch normalization layers, five fully connected layers, and four dropout layers, with activation functions termed ReLU and linear. The numbers of filters in the convolutional layers were 12, 24, 48, and 96, with the sizes of  $9 \times 9$ ,  $7 \times 7$ ,  $5 \times 5$ , and  $3 \times 3$ , respectively, containing one channel. Pooling layers took the maximum operator to extract values for a  $2 \times 2$  spatial region, with a stride equal to one. The number of neurons in fully connected layers equaled 500, 250, 100, 20, and 1, respectively. With regard to dropout layers, the probability of dropping neurons was set to 25% to prevent overfitting. Considering the model performance and time cost comprehensively, the batch size was set to 5000. The ratio of the validation dataset was 0.2 and accounted for 1,875,505 samples. The adaptive moment estimation (Adam) with the learning rate of 0.001 was selected as an optimizer, while the loss function was the mean squared error (MSE). The number of iterations was set to 60 according to the pre-experiment (when the model iterated 60 times, the best results were found at an earlier iteration), and the best configuration of the training model was saved.

#### 2.4. Model Evaluation

A training set and a validation set were used in the training process, for adjusting and initially evaluating the model. The test set was not used in the training or optimization steps; it was only used to evaluate the generalization ability of the model. The real performance of the model would generally be overestimated using cross-validation, and if the data in the test set were not totally independent from the training set, it would lead to misunderstanding the evaluation as well [71]. A method similar to the leave-one-out cross-validation method was adopted to estimate the model performance. Data was selected in any 6 months from the 7 overlapping months to train the model, and the data in the remaining one month was used as the test set to evaluate the generalization ability of the model. The number of training sets and test sets was 8,037,882 and 1,339,647, respectively, in each evaluation.

#### 2.5. Linear Model

In order to test the improvement of the accuracy of the CNNs regression model results, the results of the linear regression model were used as a benchmark, evaluated by the

same leave-one-out cross-validation method. The expression of a linear regression model is shown in (1):

$$y_i = k_i x_i + b_i \quad (1)$$

where  $i$  represents the pixel;  $y_i$  means the reconstructed SPOT-VGT NDVI of pixel  $i$ ;  $x_i$  means the PROBA-V NDVI of pixel  $i$ ; and  $k_i$   $b_i$  mean the regression parameters of pixel  $i$ , which was obtained by the training process.

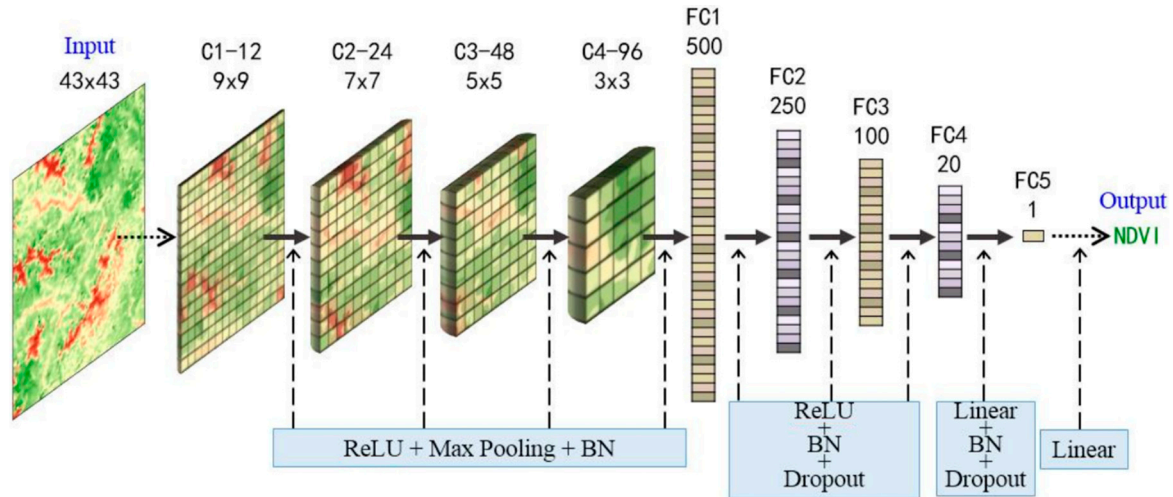


**Figure 2.** The architecture of proposed CNNs model for reconstructing multi-source NDVI. C1–C4 and FC1–FC5 represented convolutional layers and fully connected layers, respectively.

### 2.6. Linear Regression Trend Analysis

The linear time trend was calculated by regression and generally applied to estimate the temporal trend of vegetation change on a pixel scale or regional scale [72]. Based on yearly maximum NDVI on a per-pixel basis, the trends in vegetation from 1999 to 2018 were examined. This expression is shown in (2):

$$\theta_{slope} = \left( n \sum_{i=1}^n i \times NDVI_i - \sum_{i=1}^n i \sum_{i=1}^n NDVI_i \right) / \left( n \sum_{i=1}^n i^2 - \left( \sum_{i=1}^n i \right)^2 \right) \quad (2)$$

where  $n$  represents the duration,  $i$  is a sequence starting with 1,  $NDVI_i$  means the yearly maximum NDVI in year  $i$ , and  $\theta_{slope}$  is the trend of NDVI. The vegetation changes positively with the value of  $\theta_{slope}$  greater than 0, while  $\theta_{slope}$  less than 0 indicates the degraded trend of vegetation.

### 2.7. Soil Quality Measurement

In order to explore the correlation between soil quality and post-earthquake vegetation coverage recovery, 8 groups of 16 soil samples in the study area were selected. One of the sampling points in each group was from the denuded area, and the other was a control point (non-denuded) close to it. The selection of samples also followed the principles: the soil was stable with small human disturbance; the soil damage was due to the Wenchuan earthquake and its secondary disasters. The soil samples in 2011 and 2018 were collected for laboratory analysis, and the soil moisture, soil bulk density, total nitrogen (Total N) and available nitrogen, total phosphorus (Total P), available phosphorus (Available P), total potassium (Total K), available potassium (Available K), and organic matter content were measured.

### 2.8. Correlation Measure of Human Activity Intensity and NDVI

To analyze the relationships between vegetation recovery and human activities, the land use types in the study area were counted for 2018 (excluding areas of water bodies),

farmland and constructed land were classified as “human-dominated” type, woodland and grassland as “nature-dominant” type, and the “unused” type that generally refers to mountain peaks and denuded areas. The area ratios of these three types are counted at different NDVI slope levels ( $\theta_{slope}$ ).

### 3. Results

#### 3.1. Long-Term Series NDVI Reconstruction

##### 3.1.1. Model Evaluation and Data Reconstruction

Table 2 compares the performance of CNNs and the linear model. The leave-one-out cross-validation results of CNNs for reconstructing multi-source NDVI were steady across the months. It demonstrated good predictive performance of the CNNs model, the  $R^2$  ranging from 0.776 to 0.884, with a mean of 0.819. CNNs model performed much better in predicting and generalizing, while the linear regression model was unable to predict negative NDVI changes. Based on the monthly maximum PROBA-V NDVI from June 2014 to December 2018, the well-trained CNNs model was used to predict the monthly maximum SPOT-VGT NDVI, which was used to generate the complete SPOT-VGT NDVI time series from 1999 to 2018. Then the yearly maximum SPOT-VGT NDVI time series was composited for the study area to understand vegetation changes.

**Table 2.** Results of leave-one-out cross-validation for CNNs and linear model.

Date Index	Model	2013-11	2013-12	2014-01	2014-02	2014-03	2014-04	2014-05
$R^2$	CNNs	0.884	0.846	0.857	0.790	0.796	0.776	0.781
	Linear	0.783	0.756	0.748	0.722	0.714	0.723	0.721
Slope	CNNs	0.886	0.889	0.879	0.764	0.899	0.819	0.836
	Linear	0.794	0.778	0.764	0.664	0.776	0.780	0.774
Min Bias *	CNNs	0.027	0.048	−0.04	−0.037	0.065	0.02	−0.013
	Linear	0.109	0.108	0.106	0.126	0.111	0.070	0.071
Max Bias *	CNNs	0.03	−0.002	−0.056	−0.025	−0.006	−0.079	−0.024
	Linear	−0.109	−0.106	−0.108	−0.113	−0.092	−0.105	−0.100

\* Bias < 0 indicates underestimation: The predicted value is lower than the observed value; Bias > 0 indicates overestimation: The predicted value is higher than the observed value.

##### 3.1.2. Comparisons to Reconstructed NDVI

There were no large-area devastating disasters that occurred between 2013 and 2018, thus the intra-annual characteristics of vegetation change are expected to remain similar during these years. The comparison of NDVI products from different satellites was inconsistent due to their nonlinear differences. Therefore, the average monthly maximum SPOT-VGT NDVI in 2013 was selected as a reference to validate the accuracy and continuity of reconstructed data. We concluded that the intra-annual change in the predicted NDVI was consistent with the observed NDVI, and the average monthly maximum NDVI between 2014 and 2018 fluctuated normally compared with the same month in 2013 (Figure 3). Consequently, it was accepted that the CNNs reconstructed SPOT-VGT NDVI model in the study area was reliable.

MODIS NDVI has long time spans and multi-sensor data sources. Correlation calculations with MODIS NDVI on Terra and Aqua sensors examined the trend consistency and local variability of SPOT-VGT NDVI on an interannual scale. Figure 4 compares reconstructed SPOT-VGT NDVI and MODIS NDVI of different sensor Terra and Aqua from 2003 to 2018, which avoided possible errors caused by the SPOT satellite VGT sensor calibration. The values of both resources of MODIS NDVI were higher than SPOT-VGT NDVI, but the trends were consistent and the NDVI data of each sensor were internally consistent. The inter-annual trend of reconstructed SPOT-VGT NDVI with MODIS NDVI (Aqua) had positive correlation with a correlation of 0.656 (99% confidence level) and 0.699

with MODIS NDVI (Terra), which was in line with the conclusions of previous studies on the relatively large differences between these two data sources in Southwest China [47]. The local differences between reconstructed SPOT-VGT NDVI and MODIS NDVI were mainly reflected in 2009, 2012, and 2018. The possible reason is that MODIS sensors tended to saturate the NDVI of the forest, which is the main cover type in the study area [26,73], and their higher cloud pollution compared with SPOT-VGT product [36].

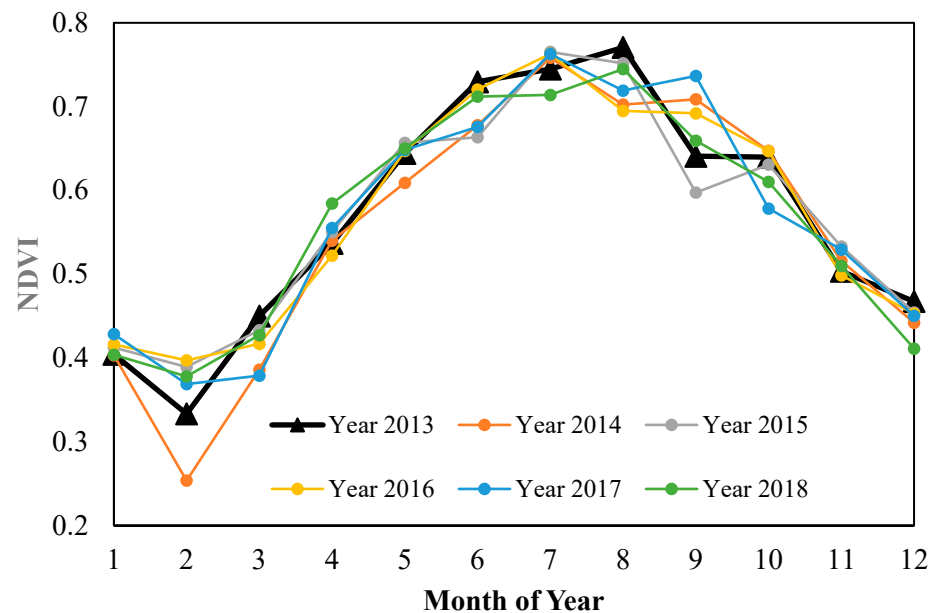


**Figure 3.** Intra-annual comparison between reconstructed (Year 2014 to 2018) and observed (Year 2013) NDVI of SPOT-VGT.

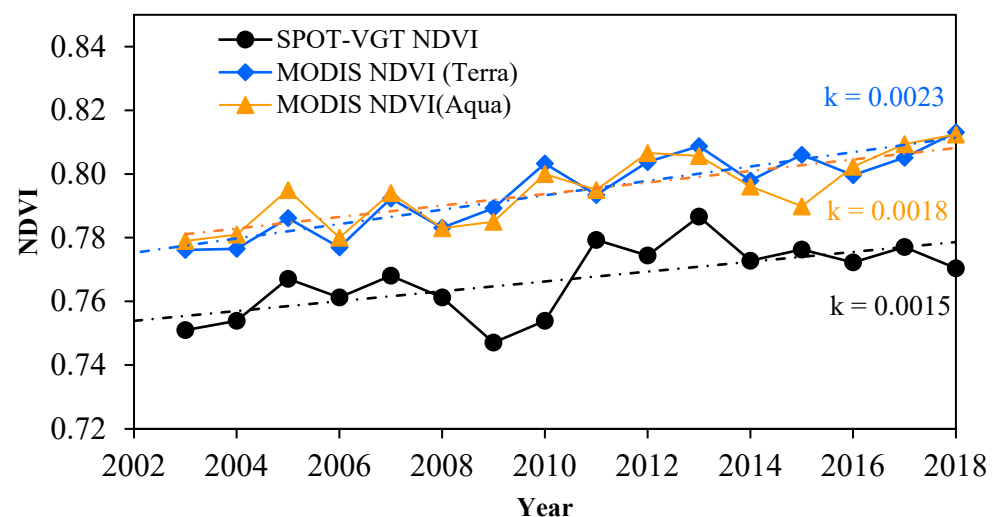


**Figure 4.** Comparisons between reconstructed SPOT-VGT NDVI and MODIS NDVI from Terra and Aqua collection. “k” refers to the slope of the linear fit of NDVI increasing.

### 3.2. Spatiotemporal Patterns of Vegetation Change

#### 3.2.1. Temporal Patterns

From 1999 to 2018, NDVI in the worst-hit areas of the Wenchuan earthquake showed an increasing trend, but had obvious decreases in 2000 and 2008 (Figure 5). The Grain for Green Project, a program to reduce forest removal and return cultivated land on steep slopes ( $\geq 25^\circ$ ) to forestlands in the upper Yangtze River Basin started in the study area in 1999. While still in the early stage of the project at the time of the earthquake, the large surface disturbances in areas with low forest cover caused intensified soil erosion and a

decrease in vegetation cover. Afterward, trees grew and the land surface recovered, leading to an increase in NDVI in subsequent years [74,75]. In addition to the positive effects of returning farmland by natural succession to forest, the large increase in NDVI from 2002 to 2003 seen in Figure 5 appear to be affected by the difference in spectral response functions between SPOT VGT-1 and VGT-2. This sensor difference caused a reflectance difference of 2.1% and 6.3% respectively for B2 (red band) and B3 (near-infrared band), resulting in an increase of 3.4% in the observed NDVI ( $NDVI > 0.3$ ) [47,76]. In the period before and after the earthquake (2003–2011), the NDVI changes show three obvious phased characteristics. The Natural Succession stage (2003–2007, P1): The vegetation during this period was not subject to a significant destructive disturbance event, and thus the interannual trend in NDVI increased. The Continuous Degradation stage (2007–2009, P2): During this phase, the rate of degradation exceeded the increasing rate of NDVI from the previous pattern of normal succession. The Wenchuan earthquake in 2008 caused severe surface disturbances and serious damage to surface vegetation, leading to a significant reduction in NDVI. Due to secondary disasters like landslides and debris flows, the NDVI across the whole region showed greater degradation in 2009 than in 2008. The negative effect of the earthquake on vegetation is persistent and shows a pattern of hysteresis in recovery [77,78]. In the Rapid Recovery stage (2009–2011, P3): Vegetation cover recovered, with a steeper rate of growth than the succession before the earthquake, up to about the value that would have intersected the earlier slope of increasing NDVI before the earthquake. Destruction and rapid recovery were common occurrences in the study area after the earthquake. As shown in the maps in Figure 5, unlike the relatively balanced NDVI increased and decreased areas in P1, the degradation in P2 and the increasing in P3 had wider areas, which were 70% area in P2 and 85% in P3, respectively. From 2009 to 2010, the increment of NDVI increase was relatively small, but by 2010, succession and recovery of the damaged vegetation occurred along with increased soil stability and soil water-holding capacity as vegetation cover increased, showing a significantly greater rate of growth in the late stage of recovery (2010–2011). Vegetation showed fluctuations dominated by phenological factors in 2012–2018. NDVI reached its maximum value in 2013 and then decreased, which is related to the sudden increase in temperature and precipitation in 2013 (Figure S1). The correlation between NDVI, annual total precipitation, and annual mean temperature in this period was higher than that of other periods, which are 0.635 and 0.602 (90% confidence level), respectively. While NDVI is a good indicator of a change in vegetation greenness, it generally does not provide enough information to identify the cause of change and it has limited capacity to identify changes in species composition without field data. Because we lacked data to document changes in species composition, we did not specify changes in species distribution. It is likely that the enhanced growth observed in the 2010–2013 period is partly or strongly related to colonization by early successional species, including invasive species, in the previously denuded hill slopes. These species are expected to be gradually replaced over a few years by the native tree and shrub species, if no new severe disturbances reset the recovery. The decreased NDVI after 2013 may indicate such a transition has started, independent of the impact of the less favorable weather at this time.

### 3.2.2. Spatial Distribution of Vegetation Cover

Although the average NDVI of the entire study area showed an upward trend from 1998 to 2018, the characteristics of vegetation cover changes varied in spatial distribution. (Figure 6a). The areas where vegetation improved, was maintained, or degraded in the study area accounted for 48.06%, 47.72%, and 4.22% of the total area, respectively. The vegetation improved across most of the northeast, and the slope was more positive in the southwest than in the core area, and the positive evolution of the vegetation in the Jialing River Basin was strongest. Degradation of vegetation mainly occurred in three regions: (1) The high mountain areas of Northeast China, especially the junction of Minjiang River Basin and Dadu River Basin. This area has a high elevation ( $>4000$  m), and its ability to support rapid growth of vegetation is limited. Therefore, from 1999 to 2018, the NDVI of

the high-elevation area at the boundary of the two watersheds had maintained a low value and even showed a trend of degradation. (2) The epicenter and surrounding fault zone. The huge power released in the seismic wave destroyed extensive surface structures including both vegetation, buildings, roads, and other structures, triggering massive landslides and rock avalanches as well as impounded rivers, which was followed on hillslopes by water loss and soil erosion that further decreased vegetation growth and plant cover, and facilitated its re-destruction by secondary disasters like debris flows and landslides. (3) Residential and farming areas, primarily in the southeastern region, such as near Chongzhou and Pengzhou. Urban settlements, agricultural construction, cultivation, and other human activities were significantly impacted, and an impermeable soil layer often replaced the original vegetation and soil cover that were lost after the earthquake.

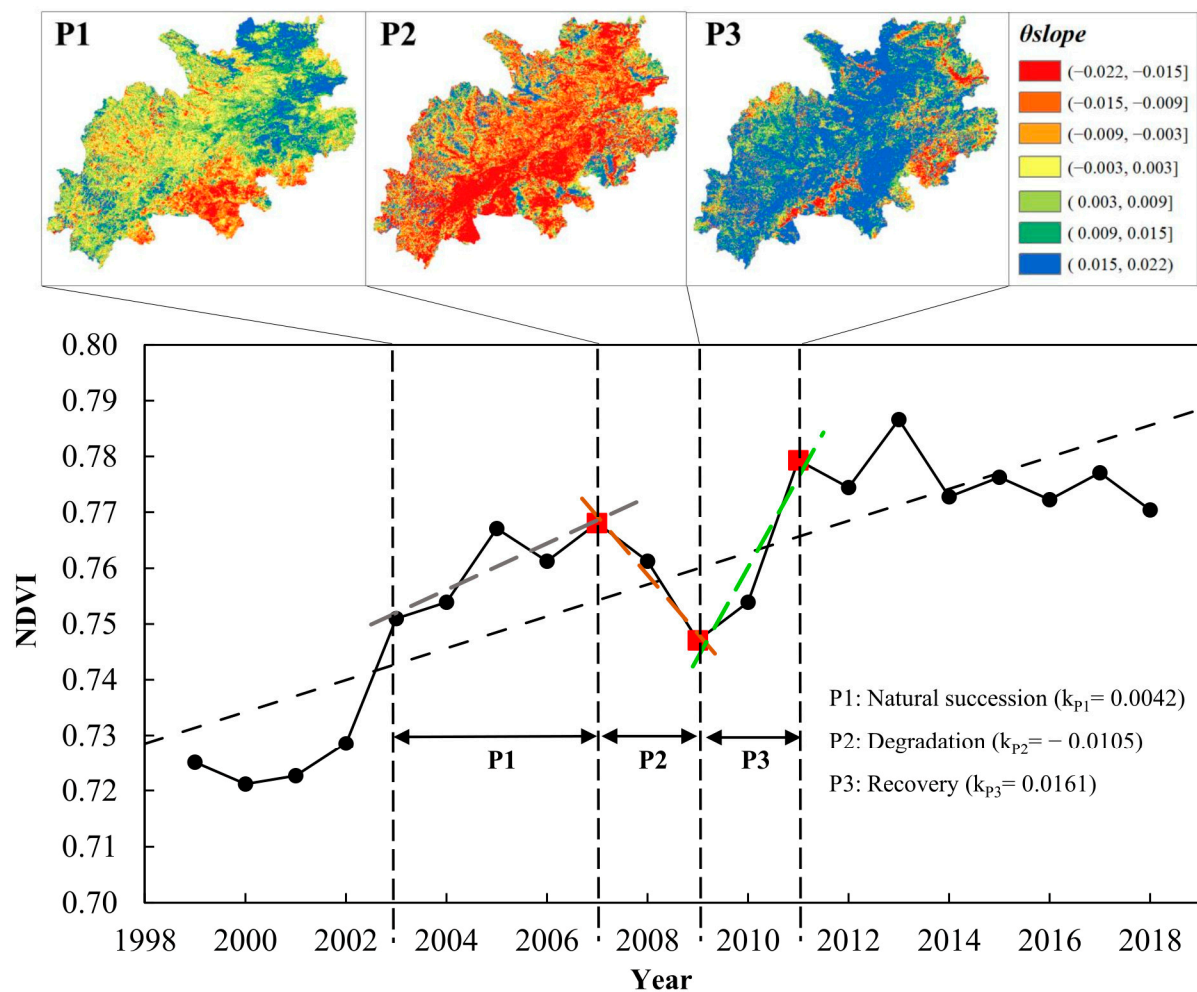


**Figure 5.** Inter-annual variation of NDVI in the study area. P1, P2, and P3 represent three periods of the pre-earthquake natural succession, post-earthquake degradation, and rapid recovery of NDVI in the study area, respectively. The corresponding  $k$  refers to the slope of the NDVI linear fit within the period.

In order to better represent the impact of the earthquake on vegetation growth, the vegetation growth trend of the study area is divided into 10 years before the earthquake (1999–2007, Figure 6b) and 10 years after the earthquake for comparison (2009–2018, Figure 6c). Before the earthquake, vegetation in most parts of the study area generally showed growth, especially in the Longmen Mountain area (epicenter and surrounding fault zone) and the northeast area. However, after the earthquake, there appeared contiguous areas of degraded vegetation that were not there before; Figure 6. Two regions: the alpine high-elevation region in the northeast, and the residential and farming areas, primarily in the southeast, showed negative growth in both periods of 1999 to 2007 and 2009 to 2018,

which are the same as the trend in the whole study period. The regions of the epicenter and surrounding fault zone had the fastest growth rate after the earthquake. This is in line with the curve of the rapid Recovery Period in Figure 2. However, the boundary regions of the Dadu River basin, Minjiang River Basin, and Fujiang River basin performance became worse in vegetation growth after the earthquake, especially in Wenchuan, Lixian, and Pingwu. According to Duan et al. [1], who researched the ecosystem service based on Net Primary Productivity (NPP), the changes in ecosystem services in Wenchuan and Lixian were climate-dominated, while Pingwu was dominated by mixed factors (climate, disasters, and human activities). Referring to the change of its driving force, the declines of NDVI in Wenchuan and Lixian (vegetation continued to be destroyed or recovered slowly) were mainly dominated by climate factors. Minjiang River Basin contains a large number of high-elevation areas and dry-hot valley areas, and these two were the key factors that cause frequent debris flows and landslides [79,80]. Therefore, after the earthquake disturbance, this area is more likely to experience re-damage, which further hinders the post-earthquake recovery of vegetation. For Pingwu, it was the high proportion of cash crops was considered [81]. The recovery of the economic crop was closely related to human activities and quite different from natural succession, which may be the reason for the hindered restoration of NDVI.

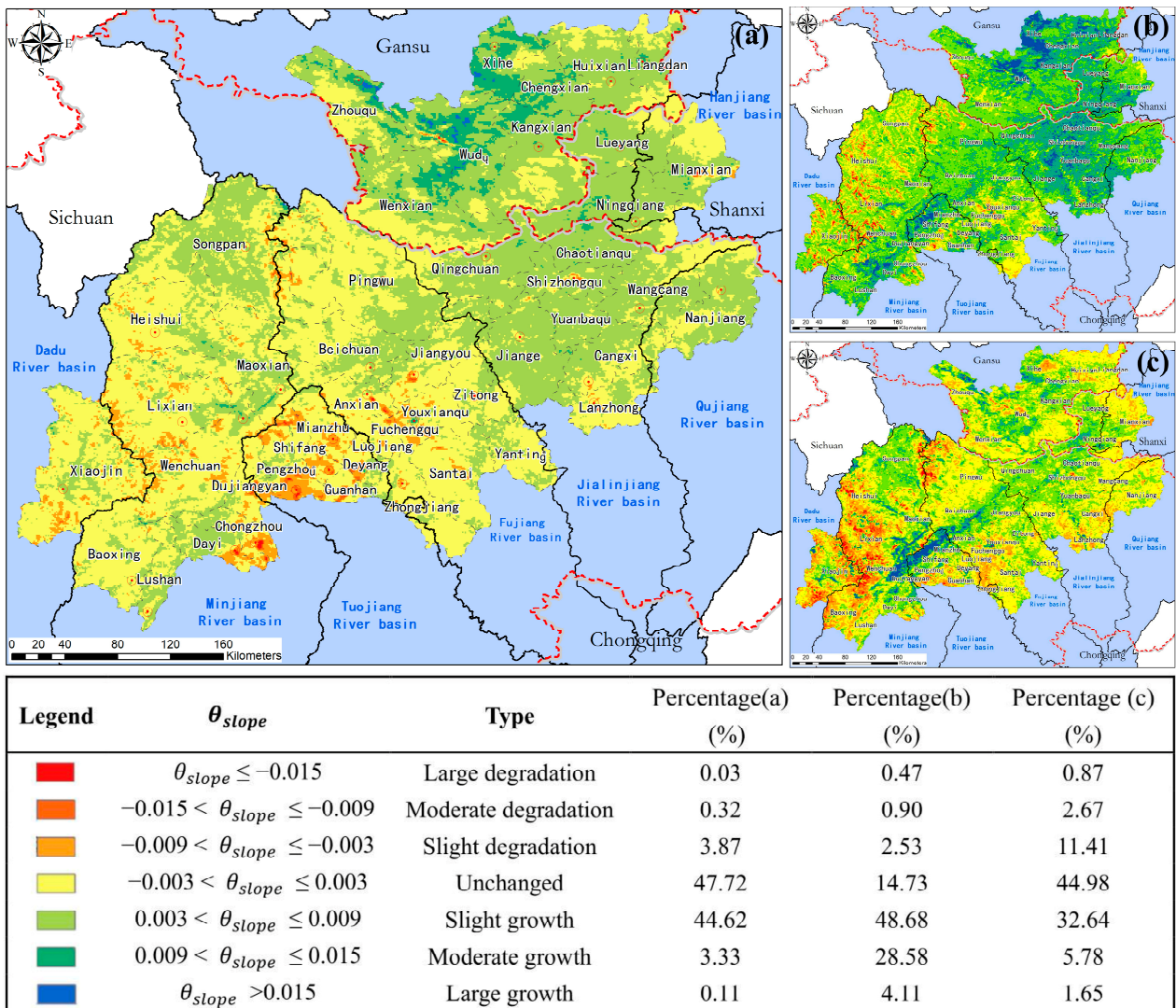


Figure 6. Spatial distribution of changes in the slope ( $\theta_{slope}$ ) of NDVI (a) from 1999 to 2018, (b) 1999 to 2007, and (c) 2009 to 2018.

### 3.3. Vegetation Recovery Patterns after the Earthquake

#### 3.3.1. Year of Initiation of Recovery

Vegetation recovery is the process of natural succession after the destruction caused by the earthquake and the following geohazards. Although the vegetation recovered in most parts of the worst-hit areas of the Wenchuan Earthquake and was even better than it was in 1998, the earthquake caused a lag in the vegetation growth in the core area, relative to the surrounding area. In order to evaluate the patterns of vegetation recovery on a pixel scale, the initiation of vegetation recovery was calculated on a pixel scale. The initiation of vegetation recovery is the year corresponding to the first time the pixel reached or exceeded the 2007 level after the earthquake. The baseline for restoration is the vegetation coverage level before the earthquake ( $NDVI_{2007}$ ). Specifically, for pixel A, its  $NDVI_{2008} \geq NDVI_{2007}$ , then the initiation of vegetation recovery of A is 2008, and the degradation time is 0, which means that the vegetation has not been significantly damaged, or the damage has been restored in the same year. Analogously, for pixel B, if its  $NDVI_{2009} \geq NDVI_{2007} > NDVI_{2008}$ , then the initiation of vegetation recovery of pixel B is 2009 and the degradation time is 1, which means that the vegetation coverage after the earthquake showed degradation in 2008 and improved for the first time in 2009. However, due to the phenomenon of “damage, recovery, re-damage, recovery” in some landslides and debris flow area, the recovery initiation in this study is the first year that reaches or exceeds  $NDVI_{2007}$ , and the subsequent years will not be repeated statistics. Affected by finer-scale secondary disasters and human activities, the vegetation recovery characteristics had obvious temporal and spatial differences (Figure 7), which also shows its environmental vulnerability. The earthquake caused a decrease in vegetation cover over 51.66% of the study area, while the rest of the area (48.35% of total, part of them recovered in 2008) had NDVI values consistent with 2008 vegetation levels in the region. The NDVI in the northwest and southeast were degraded for only a short period, and the vegetation restoration lagged by 1 year (2009). The regions with a lag of 2–3 years are concentrated in Longmen Mountain seismic fault zone and other fault zones. These regions have active geological movements and complex topography and not only did they suffer the greatest impact in the 2008 Wenchuan Earthquake but are also most prone to multiple secondary disasters. As a result, the surface was repeatedly damaged, hindering the recovery of vegetation restoration, which may cause these sites to undergo an ecosystem shift and enter a degraded alternate state. Most of the southeast basin where NDVI levels recovered later are close to urban and agricultural sites and other human activities, suggesting interference may be another main reason for the slow recovery of vegetation cover. The statistical percentage clearly shows that greater than 48% of pixels (greatest area) showed recovery that began in 2008. By 2011 and after, only about 5% of the area remained to initiate recovery, which is less than 1% of the whole study area.

#### 3.3.2. Recovery in the Decade after the Earthquake

The earthquake caused a massive disturbance in local ecosystems, especially within the fault zone. The vegetation level in the Longmen Mountain area dramatically decreased in 2008 and did not recover to the level of surrounding pixel values (Figure S2). As shown in Figure 6c, the Longmen Mountain area had the fastest growth rate after the earthquake, but the rapid growth of NDVI represents recovery from severe damage rather than restoration to pre-earthquake levels or restoration to pre-earthquake forest species composition. Figure 8 shows the results of NDVI values in 2018 minus NDVI values in 2007 (the last year before the earthquake). It is worth noting that the NDVI of the Longmen Mountain fault zone had not recovered to the pre-earthquake level of 2007 by 2008, even though this area had the fastest recovery rate (Figure 6c). In this situation, it is necessary to fully consider the denuded area caused by multiple geological disasters for vegetation restoration planning.

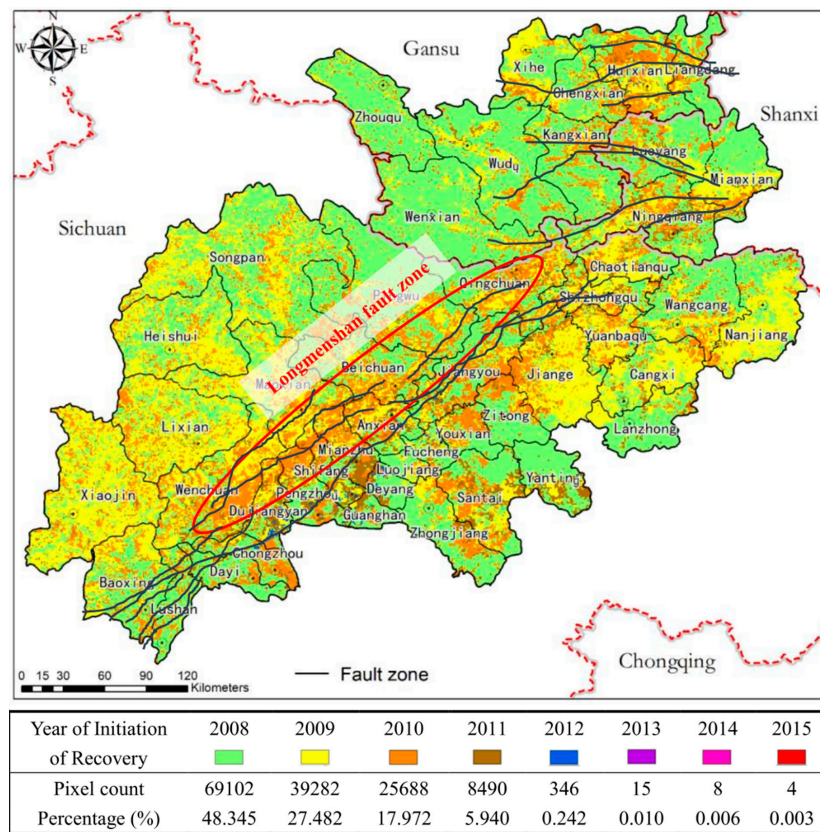


Figure 7. Mapping about the year vegetation recovery was initiated in the study area. Fault zone data referred to Atlas of Mountain hazards and soil erosion in the Upper Yangtze [82].

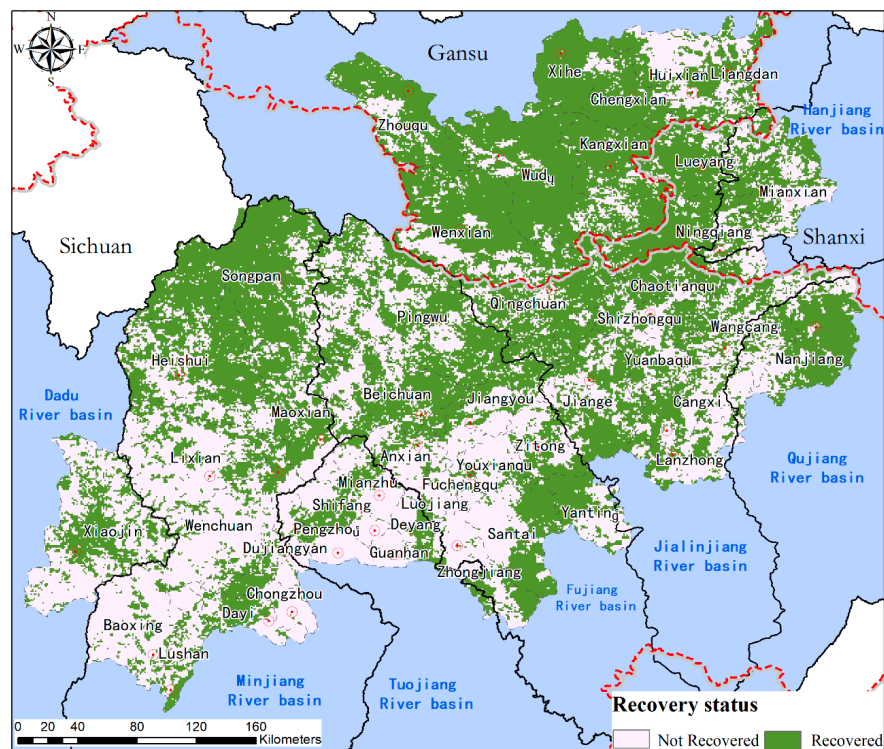
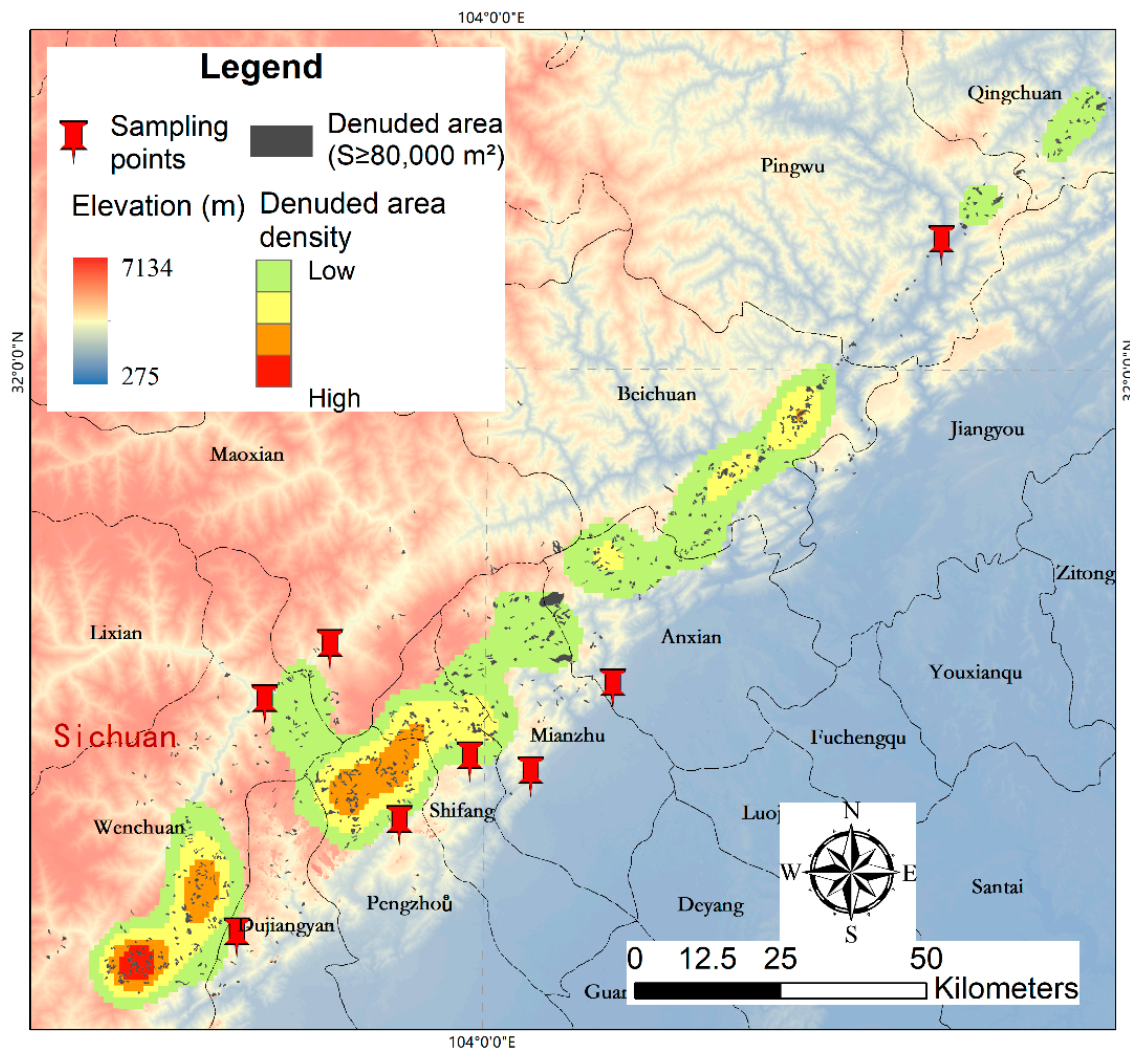


Figure 8. Recovery status in the decade (2018) after the earthquake (based on the pre-earthquake level of 2007).

### 3.3.3. Obstructed Recovery in Denuded Area

After the Wenchuan earthquake, a large number of debris flows and landslides occurred annually in the affected area during the annual monsoon period (June to September), which caused the re-activation and migration of surface sources [9]. A total of 879 denuded areas ( $S \geq 80,000 \text{ m}^2$ , Figure 9) were selected as typical disturbance examples based on remote-sensing images and data resolution [44,83]. Eight groups of soil quadrats were sampled for soil quality monitoring (Figure 9) and each group of soil quadrats contained soil samples from denuded areas and non-denuded areas in both 2011 and 2018.



**Figure 9.** Denuded areas ( $S \geq 80,000 \text{ m}^2$ ) and sampling locations.

The change in NDVI in the denuded area showed three stages that were similar to patterns in the larger study area: natural succession, continuous degradation, rapid initial recovery, and the after earthquake recovery hysteresis. Compared to the overall changes in the study area, natural succession recovered relatively better than in the denuded areas ( $k_{LP1}: 0.0060 > k_{P1}: 0.0042$ ). In the more severe areas of vegetation degradation ( $k_{LP2}: 0.0893 < k_{P2}: 0.0105$ ), the worst areas are located where more significant geological disasters occurred and where the recovery was more rapid ( $k_{LP1}k_{LP3}: 0.0401 < k_{P3}: 0.0161$ ). However, by 2018, NDVI had not fully recovered to its pre-earthquake level (Figure 10). Compared with areas that did not experience subsequent severe disturbances, areas that had multiple denuding events had a greater decline in NDVI, a longer recovery time, and a delayed start in vegetation recovery by several years (Table S2).

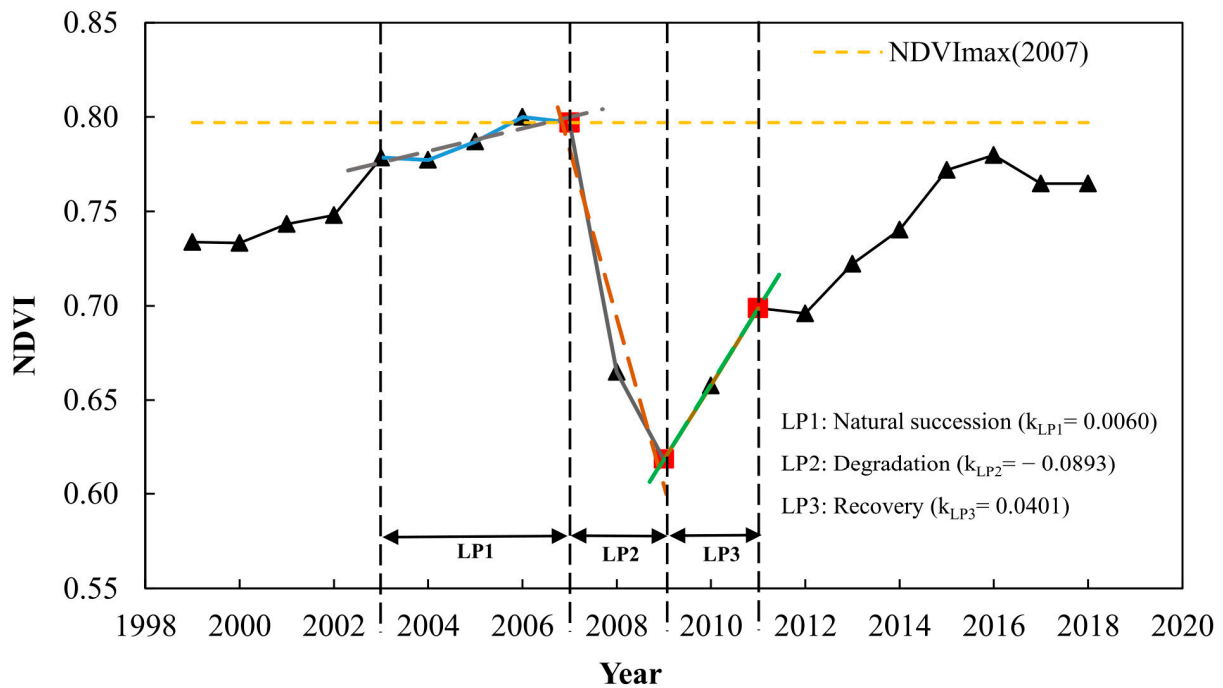


**Figure 10.** Interannual variation in NDVI in denuded areas ( $S \geq 80,000 \text{ m}^2$ ). LP1, LP2, and LP3 represent three periods of pre-earthquake natural succession, post-earthquake declines, and recovery of NDVI in the denuded (landslides) areas, respectively. The corresponding  $k$  refers to the slope of the NDVI linear fit within the period.

Comparing the soil quality between 2011 and 2018 at the same location, Figure 11 showed that soil quality in the non-denuded impacted area was generally better than in the denuded area, especially the availability of essential macronutrients, and characteristics generally indicating better soil health. The decrease in soil quality in the denuded areas may reduce survival in these areas for species with slower growth rates.

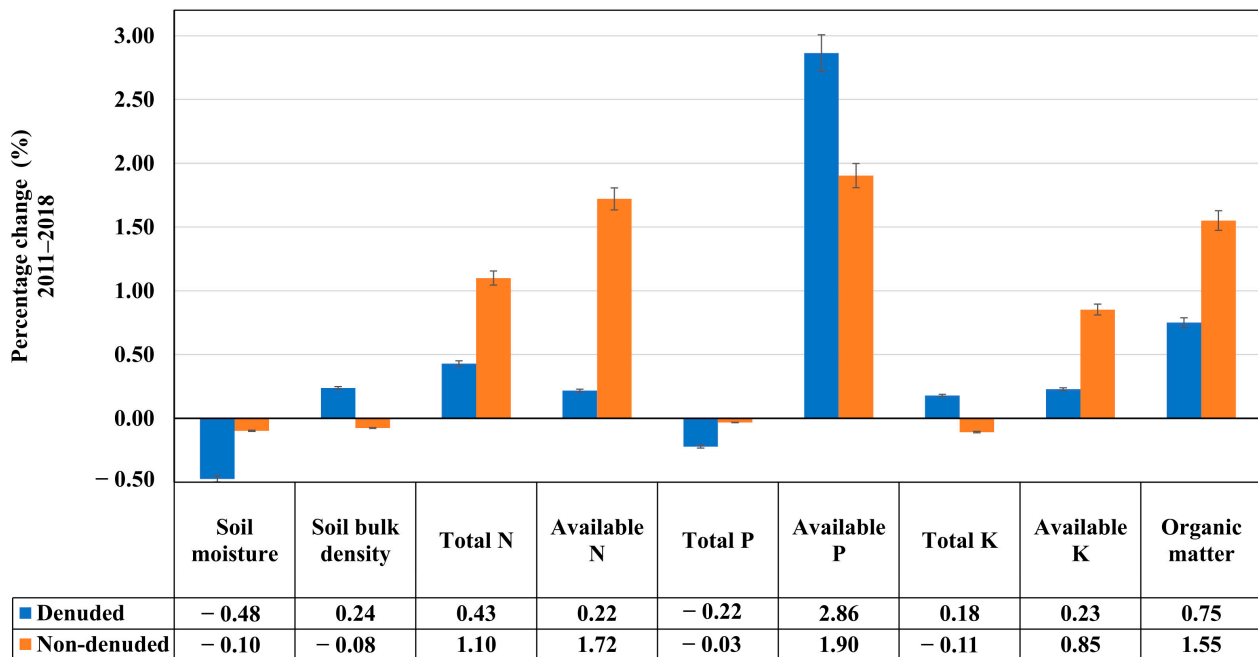


**Figure 11.** Comparison of soil quality between denuded area and non-denuded area.

The areas that retained the topsoil and surface structure have significantly higher total nitrogen, available nitrogen and potassium, and organic matter compared to areas impacted by destructive geological disasters. They also retain higher soil moisture and lower bulk density. Altogether, these soil patterns are found in areas that did not experience secondary destructive geo-hazards and are associated with better growth and more rapid vegetation recovery.

In order to improve vegetation management for the denuded areas, we calculated the vegetation recovery time based on the NDVI regression model (Figure 6c) after the earthquake starting with the lowest value of NDVI (2009). In the denuded areas, the average recovery time was 10 years with a standard deviation of 10 years. These results indicate that without active restoration: (1) part of the vegetation in the denuded area started recovery soon after the earthquake; (2) most of the denuded vegetation (67.12% of the total denuded area) recovered by 2018; (3) the 10-year standard deviation plus the average indicates that the vegetation is expected to take 20 years to return to the pre-earthquake (2007) levels.

### 3.4. Relationship with Vegetation Change and Other Factors

#### 3.4.1. Vegetation Changes in Elevation Belts

The parts of the study area with low-NDVI and declining rates of vegetation growth are in both high-elevation and low-elevation areas, so NDVI was evaluated by an elevation belt (Figure 12). Overall, vegetation showed the highest levels of NDVI at elevations between 800 to 1550 m, and lower NDVIs (0.65 to 0.80) at lower elevations (below 800 m), which were negatively affected by human habitation and farming. It can be seen from Figure 1 that the low elevation areas are mainly distributed in the southeastern part of the study area, especially in the southern areas with many cities close to the Chengdu Plain. Strong human activities in these low-elevation areas made the NDVI of urban land and farmland lower than NDVI of middle-elevation forests, and it could be supported by the long-term annual NDVI values (Figure S2) and low growth rates of NDVI in a human-dominant area (Figure 13). At extremely high elevations, alpine vegetation has low stature dwarf shrubs with low canopy cover, which relates to the poor soil, short growing season, extremely cold winters, and frequent cloud cover reducing sunlight intensity. It is worth noting that the earthquake caused the vegetation level to dramatically decrease across most elevations in 2009, and vegetation in most elevations started recovering within 1–2 years after the Wenchuan Earthquake, which is confirmed by the pixel scale analysis shown in Figure 7. In addition, the vegetation level benefited from increased precipitation for a longer period, with a continuous NDVI increase, especially in 2013 when the precipitation conditions were the highest (Figure S1).

#### 3.4.2. Vegetation Change in Different Land Use Types

The other region that demonstrated decreasing vegetation cover is in the low-elevation regions of the Mingjiang River watershed and the Tuojiang watershed, which is close to Chengdu, the capital of Sichuan Province. This region has been impacted by the expansion of the city of Chengdu, with low-elevation land use changing from farming to construction. There are other small towns that have also contributed to the land cover change. Correlation analysis between land use types and NDVI changes can reveal the impact of human activity intensity on vegetation cover. It can be seen in Figure 13 that the regions with the most negative  $\theta_{slope}$  NDVI have the least in the human-dominant land type. A positive trend in NDVI always exists in regions with a significant nature-dominant land ratio. Unused land throughout the region has a negative trend in NDVI, which is located primarily in high-elevation regions.

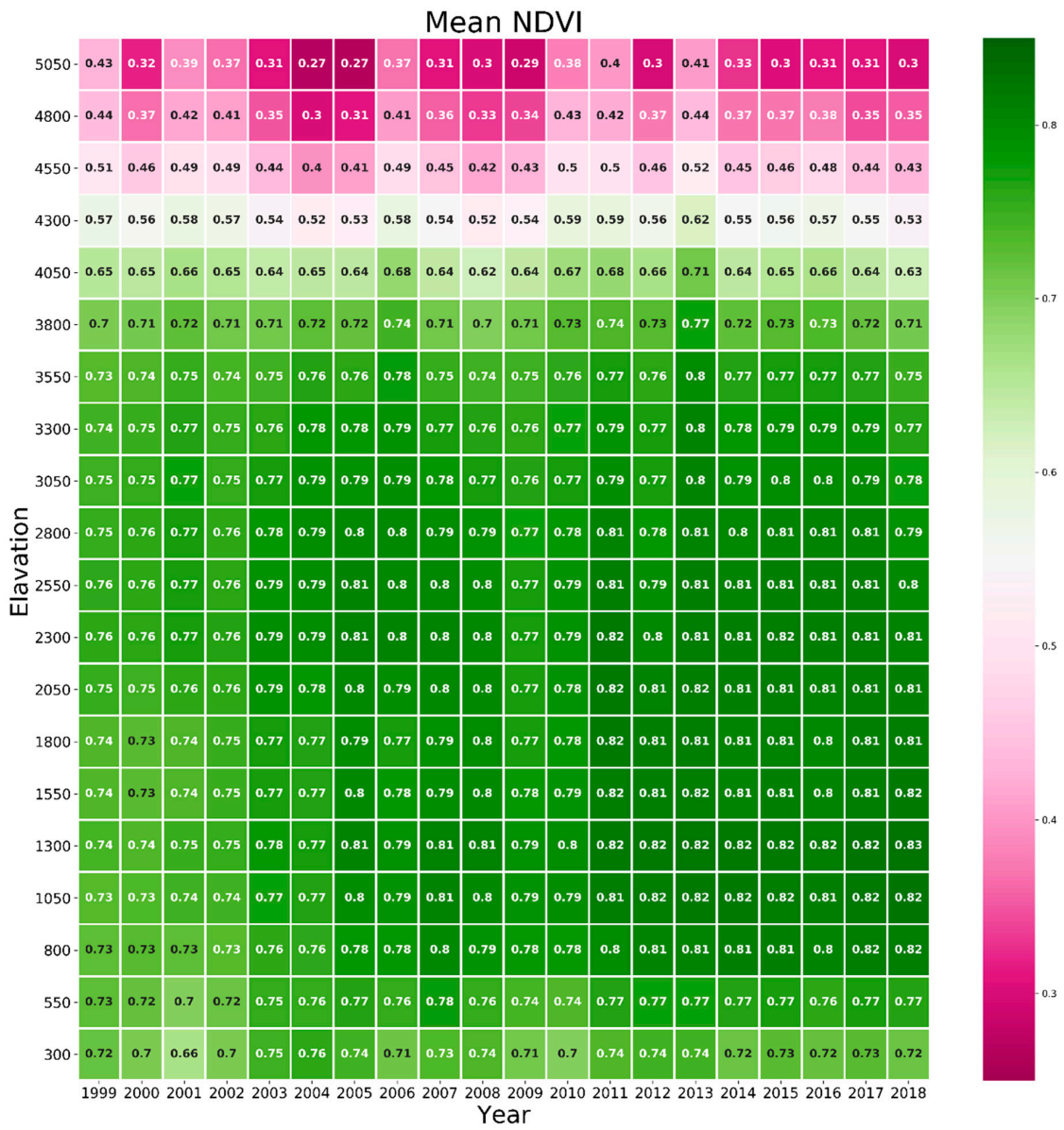


Figure 12. NDVI from 1999 to 2018, at elevations between 250 m and 6000 m.

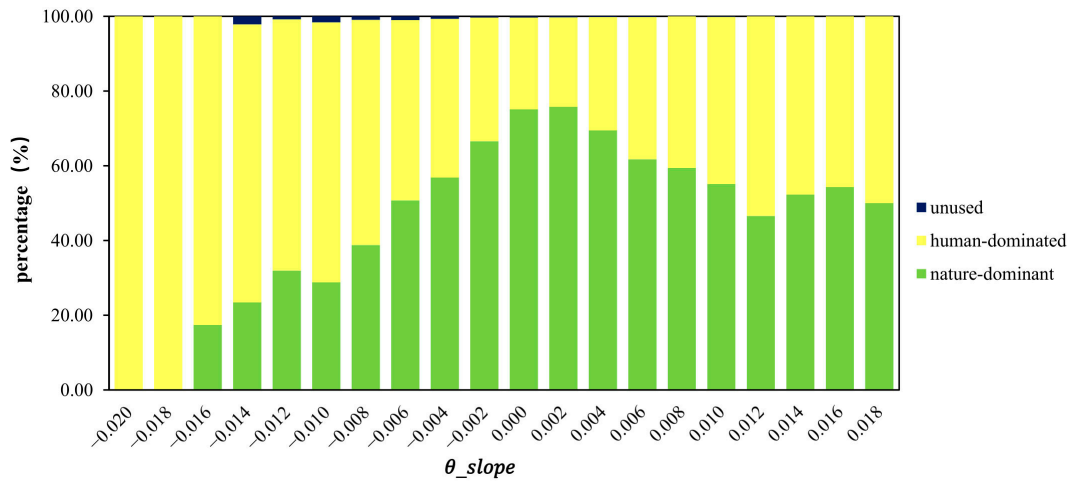


Figure 13.  $\theta_{slope}$  of the annual NDVI for different land use types.

#### 4. Discussion

The research on vegetation restoration after disturbance is diverse, and the vegetation recovery model includes a restoration trend, restoration starting point, restoration prediction, and so on. According to the results of our vegetation recovery in this study, 48% of damaged areas with loss of vegetation cover showed that the initiation of revegetation and recovery was after 1 year, in 2008, and by 2013 more than 99% of the severely damaged land had started recovery. Liu et al. [84] investigated vegetation recovery and found that it started soon after the earthquake across the entire affected area, and areas with greatest damage had recovered to 84% and 87% after 1 and 2 months later, respectively. Typically, these are early successional species that exhibit rapid seed sprouting, like grasses and herbs, species that can regrow from rhizomes, or woody species that stump sprout. Most mid- and upper-elevation forest species have a seed pool in the soil that sprout in spring, and thus are likely delaying germination until 2009 or later. Jiang et al. [81] concluded that it took until 2013 for 41% to be restored to the level before the earthquake. These differences are due to the different definitions of recovery and the conditions of the specific study area. It must be noted that identical NDVIs only indicate that similar amounts of green vegetation were present in the two time periods. It does not report whether the composition of prior forests or shrublands had been restored. Jiang et al. [81] used the NDVI from 2013 compared to 2008 and estimated a recovery ratio much lower than that reported for this study (using the year when the NDVI value was first greater than or equal to the value in 2007 as the starting point for recovery). The difference expressed the fracture of NDVI after the initiation of recovery, caused by phenological conditions or geo-hazards.

The regions of repeated geo-hazards show an unhealthy trend of vegetation cover. Geo-hazards caused by earthquakes have been demonstrated to have an increasing negative impact on ecosystems by the vicious circle observed in the Wenchuan earthquake area. Damage to the ground structure during the earthquake destroys the habitat for vegetation and increases water loss and soil erosion caused by vegetation degradation and loss, which leads to further ecosystem function decline [10,85]. Yang et al. [86], Yunus et al. [44], and Chen et al. [87] predicted that the impact on regional post-seismic landslide frequency will disappear within 20, 18, and 25 years after the Wenchuan earthquake, respectively. The NDVI trend in the denuded area and our soil investigation showed the challenge to vegetation recovery in the secondary-disaster area. NDVI in some denuded areas (32.88% of the total in this study) had not recovered to the pre-earthquake level by 2018 (10 years after the earthquake). Zhong et al. [88] showed a similar conclusion of vegetation recovery (about 60% recovered in ten years) and full recovery is forecast for 20 years after the earthquake.

As a natural disturbance, the earthquake did not completely destroy the growth of vegetation; factors that affect phenological conditions (temperature and precipitation) should be taken into consideration as drivers of primary productivity in the model for vegetation growth and recovery [89]. The NDVI value rapidly increased across the whole study area in 2013, even the denuded area showed the increasing trend, which reversed trends in 2012. In addition, NDVI had recovered to the level before the earthquake based on the initiation of vegetation recovery (Figure 4). Weather differences are the basic reason when compared with the temperature and precipitation of the previous year; the weather conditions in 2013 were more suitable to vegetation growth. Moreover, the geo-hazards were concentrated in isolated spots after 2013 [90], which helped vegetation recovery over the whole study area. However, NDVI shows a relative decrease from 2014 to 2018 compared to what it was in 2013, which is due to the decreases of the temperature and precipitation in these years. High-elevation areas maintained low NDVI levels and a negative growth trend during the study period, and this trend became more obvious after the earthquake, especially in the high elevation Minjiang River Basin. A large number of landslides occurred after the earthquake. In addition, the occurrence of drought and fire after the earthquake also increased the risk of regional debris flows, especially in areas where the soil was soft due to the earthquake [79,91], repeating the vicious circle of damaged–recovered–damaged, which prevents or inhibits vegetation restoration. The

unfavorable conditions for vegetation growth in the Minjiang River valley expanded after the earthquake, making it difficult for vegetation to recover. This is an indirect impact of the earthquake causing long-term damage to an ecologically fragile area. This study considered the NDVI recovery results 10 years after the earthquake and the first recovery year, but the detailed discussion on the “re-damage and re-recovery” scenario and corresponding driving force needs more attention.

Additional challenges result because the vegetation index does not show the reality of other aspects of vegetation, such as species composition, biomass, and its 3-dimensional structure, which are essential for it to maintain its ecosystem service. Therefore, field observations are an essential component of meeting the U.N.’s Sustainable Development Goal 15. Fieldwork, such as a solid investigation of forest components provides evidence of vegetation growth and ecosystem health, which will help identify the choice of remote-sensing data needed [36]. Soil monitoring is used in this study to characterize the damage by the landslides to the soil surface and the soil environment required for plant growth. However, more sites and more multi-period vegetation sampling data should be used in future research to complement remote-sensing data and reflect accurate assessments of vegetation recovery.

## 5. Conclusions

The heterogeneous NDVI dataset was reconstructed by the CNNs model and used to analyze long-term vegetation changes in the worst-hit areas of the Wenchuan earthquake. Vegetation in the study area showed an overall upward trend before the earthquake, with 48.06% improved, 47.72% maintained, and 4.22% degraded. However, the vegetation experienced a dramatic decline because of the earthquake, which followed a sharp degradation stage (2008–2009), rapid recovery stage (2009–2011), and fluctuation stage after repeated disasters, e.g., landslides and debris flows (2012–2018). Post-earthquake vegetation restoration patterns varied with environmental conditions at the local area, including geological disasters, elevation and mountainous terrain, human activities, and weather-related phenology. Among them, geological disasters have a considerable negative impact on vegetation restoration. NDVI in the denuded areas did not recover until 2018 and are only expected to reach the level of the pre-earthquake (2007) vegetation condition 20 years after the earthquake. NDVI change patterns showed the characteristics of vegetation under different environmental conditions and provided the reference for vegetation protection and management.

**Supplementary Materials:** The following supporting information can be downloaded at: <https://www.mdpi.com/article/10.3390/rs15020299/s1>, Table S1: The fitting results of convolutional neural networks and other methods for reconstructing heterogeneous NDVI; Figure S1: The characteristics of annual mean temperature and annual total precipitation in the study area; Figure S2: Annual NDVI for years 2007 to 2018 from the MVC analysis. The full images are shown for the first seven years to illustrate the continuity of NDVI across the Longmenshan fault boundary with vegetation in the surrounding area; Table S2: Statistics showing the beginning of vegetation recovery for pixels in areas experiencing large numbers of large landslides ( $S \geq 80,000 \text{ m}^2$ ).

**Author Contributions:** S.W.: conceptualization, methodology, formal analysis, writing—original draft, writing—review & editing, visualization. B.D.: conceptualization, formal analysis, writing—review & editing, funding acquisition. S.L.U.: conceptualization, methodology, writing—review & editing. M.S.W.: conceptualization, methodology. B.R.A.: writing—review & editing. R.Z.: conceptualization, writing—original draft, methodology, visualization. M.L.: investigation, formal analysis. All authors have read and agreed to the published version of the manuscript.

**Funding:** This research was funded by the National Natural Science Foundation of China, grant number 41977245, the National Key Research and Development Program of China, grant number 2020YFD1100701, the General Research Fund from the Research Grants Council, Hong Kong, China, grant number 15603920 and 15609421, and the Collaborative Research Fund from the Research Grants Council, Hong Kong, China, grant number C5062-21GF.

**Data Availability Statement:** Not applicable.

**Acknowledgments:** The authors would like to thank Jierui Li, Yanan Duan, and Lingke Qiu from Sichuan University for professional advice.

**Conflicts of Interest:** The authors declare no conflict of interest.

## References

- Duan, Y.; Di, B.; Ustin, S.L.; Xu, C.; Xie, Q.; Wu, S.; Li, J.; Zhang, R. Changes in Ecosystem Services in a Montane Landscape Impacted by Major Earthquakes: A Case Study in Wenchuan Earthquake-Affected Area, China. *Ecol. Indic.* **2021**, *126*, 107683. [[CrossRef](#)]
- Marusig, D.; Petruzzellis, F.; Tomasella, M.; Napolitano, R.; Altobelli, A.; Nardini, A. Correlation of Field-Measured and Remotely Sensed Plant Water Status as a Tool to Monitor the Risk of Drought-Induced Forest Decline. *Forests* **2020**, *11*, 77. [[CrossRef](#)]
- Poussin, C.; Massot, A.; Ginzler, C.; Weber, D.; Chatenoux, B.; Lacroix, P.; Piller, T.; Nguyen, L.; Giuliani, G. Drying Conditions in Switzerland—Indication from a 35-Year Landsat Time-Series Analysis of Vegetation Water Content Estimates to Support SDGs. *Big Earth Data* **2021**, *5*, 445–475. [[CrossRef](#)]
- Xu, C.; Xu, X.; Zhou, B.; Yu, G. Revisions of the M 8.0 Wenchuan Earthquake Seismic Intensity Map Based on Co-Seismic Landslide Abundance. *Nat. Hazards* **2013**, *69*, 1459–1476. [[CrossRef](#)]
- Xu, J.; Lu, Y. Meta-Synthesis Pattern of Post-Disaster Recovery and Reconstruction: Based on Actual Investigation on 2008 Wenchuan Earthquake. *Nat. Hazards* **2012**, *60*, 199–222. [[CrossRef](#)]
- Cui, P.; Chen, X.; Zhu, Y.; Su, F.; Wei, F.; Han, Y.-S.; Liu, H.-J.; Zhuang, J.-Q. The Wenchuan Earthquake (May 12, 2008), Sichuan Province, China, and Resulting Geohazards. *Nat. Hazards* **2011**, *56*, 19–36. [[CrossRef](#)]
- Lu, T.; Shi, F.; Sun, G.; Luo, Y.; Wang, Q.; Wu, Y.; Wu, N. Reconstruction of the Wenchuan Earthquake-Damaged Ecosystems: Four Important Questions: Reconstruction of the Wenchuan Earthquake-Damaged Ecosystems: Four Important Questions. *Chin. J. Appl. Environ. Biol.* **2010**, *16*, 301–304. [[CrossRef](#)]
- Pan, K.; Wu, N.; Pan, K.; Chen, Q. A discussion on the issues of the re-construction of ecological shelter zone on the upper reaches of the Yangtze River. *Acta Ecol. Sin.* **2004**, *24*, 617–629.
- Fan, X.; Domènech, G.; Scaringi, G.; Huang, R.; Xu, Q.; Hales, T.C.; Dai, L.; Yang, Q.; Francis, O. Spatio-Temporal Evolution of Mass Wasting after the 2008 Mw 7.9 Wenchuan Earthquake Revealed by a Detailed Multi-Temporal Inventory. *Landslides* **2018**, *15*, 2325–2341. [[CrossRef](#)]
- Wang, M.; Yang, W.; Shi, P.; Xu, C.; Liu, L. Diagnosis of Vegetation Recovery in Mountainous Regions After the Wenchuan Earthquake. *IEEE J. Sel. Top. Appl. Earth Obs. Remote Sens.* **2014**, *7*, 3029–3037. [[CrossRef](#)]
- Zhang, H.; Chi, T.; Fan, J.; Hu, K.; Peng, L. Spatial Analysis of Wenchuan Earthquake-Damaged Vegetation in the Mountainous Basins and Its Applications. *Remote Sens.* **2015**, *7*, 5785–5804. [[CrossRef](#)]
- Guo, N. Vegetation index and its advances. *J. Arid Meteorol.* **2003**, *21*, 71–75.
- Tian, Q.; Min, X. Advances in study on vegetation indices. *Adv. Earth Sci.* **1998**, *13*, 327–333.
- Cihlar, J.; St-Laurent, L.; Dyer, J.A. Relation between the Normalized Difference Vegetation Index and Ecological Variables. *Remote Sens. Environ.* **1991**, *35*, 279–298. [[CrossRef](#)]
- Mbow, C.; Fensholt, R.; Nielsen, T.T.; Rasmussen, K. Advances in Monitoring Vegetation and Land Use Dynamics in the Sahel. *Geogr. Tidsskr. Dan. J. Geogr.* **2014**, *114*, 84–91. [[CrossRef](#)]
- Pettorelli, N.; Vik, J.O.; Mysterud, A.; Gaillard, J.-M.; Tucker, C.J.; Stenseth, N.C. Using the Satellite-Derived NDVI to Assess Ecological Responses to Environmental Change. *Trends Ecol. Evol.* **2005**, *20*, 503–510. [[CrossRef](#)]
- Bradley, B.A.; Mustard, J.F. Comparison of Phenology Trends by Land Cover Class: A Case Study in the Great Basin, USA. *Glob. Change Biol.* **2008**, *14*, 334–346. [[CrossRef](#)]
- Gamon, J.A.; Field, C.B.; Goulden, M.L.; Griffin, K.L.; Hartley, A.E.; Joel, G.; Penuelas, J.; Valentini, R. Relationships Between NDVI, Canopy Structure, and Photosynthesis in Three Californian Vegetation Types. *Ecol. Appl.* **1995**, *5*, 28–41. [[CrossRef](#)]
- Gilbert, M.A.; González-Piqueras, J.; García-Haro, F.J.; Meliá, J. A Generalized Soil-Adjusted Vegetation Index. *Remote Sens. Environ.* **2002**, *82*, 303–310. [[CrossRef](#)]
- Jiang, Z.; Huete, A.R.; Chen, J.; Chen, Y.; Li, J.; Yan, G.; Zhang, X. Analysis of NDVI and Scaled Difference Vegetation Index Retrievals of Vegetation Fraction. *Remote Sens. Environ.* **2006**, *101*, 366–378. [[CrossRef](#)]
- Gitelson, A.A.; Merzlyak, M.N. Remote Estimation of Chlorophyll Content in Higher Plant Leaves. *Int. J. Remote Sens.* **1997**, *18*, 2691–2697. [[CrossRef](#)]
- Myneni, R.B.; Williams, D.L. On the Relationship between FAPAR and NDVI. *Remote Sens. Environ.* **1994**, *49*, 200–211. [[CrossRef](#)]
- Running, S.W.; Nemani, R.R.; Heinsch, F.A.; Zhao, M.; Reeves, M.; Hashimoto, H. A Continuous Satellite-Derived Measure of Global Terrestrial Primary Production. *BioScience* **2004**, *54*, 547–560. [[CrossRef](#)]
- Myneni, R.B.; Hall, F.G.; Sellers, P.J.; Marshak, A.L. The Interpretation of Spectral Vegetation Indexes. *IEEE Trans. Geosci. Remote Sens.* **1995**, *33*, 481–486. [[CrossRef](#)]
- Sellers, P.J. Relations between Canopy Reflectance, Photosynthesis and Transpiration: Links between Optics, Biophysics and Canopy Architecture. *Adv. Space Res.* **1987**, *7*, 27–44. [[CrossRef](#)]
- Sellers, P.J. Canopy Reflectance, Photosynthesis and Transpiration. *Int. J. Remote Sens.* **1985**, *6*, 1335–1372. [[CrossRef](#)]

27. Jeong, S.-J.; Schimel, D.; Frankenberg, C.; Drewry, D.T.; Fisher, J.B.; Verma, M.; Berry, J.A.; Lee, J.-E.; Joiner, J. Application of Satellite Solar-Induced Chlorophyll Fluorescence to Understanding Large-Scale Variations in Vegetation Phenology and Function over Northern High Latitude Forests. *Remote Sens. Environ.* **2017**, *190*, 178–187. [[CrossRef](#)]
28. Yengoh, G.T.; Dent, D.; Olsson, L.; Tengberg, A.E.; Tucker, C.J., III. *Use of the Normalized Difference Vegetation Index (NDVI) to Assess Land Degradation at Multiple Scales: Current Status, Future Trends, and Practical Considerations*; Springer: Berlin/Heidelberg, Germany, 2015; ISBN 978-3-319-24112-8.
29. Cao, M.; Prince, S.D.; Li, K.; Tao, B.; Small, J.; Shao, X. Response of Terrestrial Carbon Uptake to Climate Interannual Variability in China. *Glob. Change Biol.* **2003**, *9*, 536–546. [[CrossRef](#)]
30. Field, C.B.; Randerson, J.T.; Malmström, C.M. Global Net Primary Production: Combining Ecology and Remote Sensing. *Remote Sens. Environ.* **1995**, *51*, 74–88. [[CrossRef](#)]
31. Gamon, J.A.; Huemmrich, K.F.; Stone, R.S.; Tweedie, C.E. Spatial and Temporal Variation in Primary Productivity (NDVI) of Coastal Alaskan Tundra: Decreased Vegetation Growth Following Earlier Snowmelt. *Remote Sens. Environ.* **2013**, *129*, 144–153. [[CrossRef](#)]
32. Wang, R.; Gamon, J.A.; Emmerton, C.A.; Li, H.; Nestola, E.; Pastorello, G.Z.; Menzer, O. Integrated Analysis of Productivity and Biodiversity in a Southern Alberta Prairie. *Remote Sens.* **2016**, *8*, 214. [[CrossRef](#)]
33. Albarakat, R.; Lakshmi, V. Comparison of Normalized Difference Vegetation Index Derived from Landsat, MODIS, and AVHRR for the Mesopotamian Marshes Between 2002 and 2018. *Remote Sens.* **2019**, *11*, 1245. [[CrossRef](#)]
34. Bright, B.C.; Hudak, A.T.; Kennedy, R.E.; Braaten, J.D.; Henareh Khalyani, A. Examining Post-Fire Vegetation Recovery with Landsat Time Series Analysis in Three Western North American Forest Types. *Fire Ecol.* **2019**, *15*, 8. [[CrossRef](#)]
35. Díaz-Delgado, R.; Lloret, F.; Pons, X. Influence of Fire Severity on Plant Regeneration by Means of Remote Sensing Imagery. *Int. J. Remote Sens.* **2003**, *24*, 1751–1763. [[CrossRef](#)]
36. Fensholt, R.; Rasmussen, K.; Nielsen, T.T.; Mbow, C. Evaluation of Earth Observation Based Long Term Vegetation Trends—Intercomparing NDVI Time Series Trend Analysis Consistency of Sahel from AVHRR GIMMS, Terra MODIS and SPOT VGT Data. *Remote Sens. Environ.* **2009**, *113*, 1886–1898. [[CrossRef](#)]
37. Karnieli, A.; Agam, N.; Pinker, R.T.; Anderson, M.; Imhoff, M.L.; Gutman, G.G.; Panov, N.; Goldberg, A. Use of NDVI and Land Surface Temperature for Drought Assessment: Merits and Limitations. *J. Clim.* **2010**, *23*, 618–633. [[CrossRef](#)]
38. Shi, L.; Dech, J.; Liu, H.; Zhao, P.; Bayin, D.; Zhou, M. Post-fire Vegetation Recovery at Forest Sites Is Affected by Permafrost Degradation in the Da Xing'an Mountains of Northern China. *J. Veg. Sci.* **2019**, *30*, 940–949. [[CrossRef](#)]
39. Brown, M.; Lary, D.; Vrieling, A.; Stathakis, D.; Mussa, H. Neutral Networks as a Tool for Constructing Continuous NDVI Time Series from AVHRR and MODIS. *Int. J. Remote Sens.* **2008**, *29*, 7141. [[CrossRef](#)]
40. Gallo, K.; Ji, L.; Reed, B.; Eidenshink, J.; Dwyer, J. Multi-Platform Comparisons of MODIS and AVHRR Normalized Difference Vegetation Index Data. *Remote Sens. Environ.* **2005**, *99*, 221–231. [[CrossRef](#)]
41. Song, Y.; Mingguo, M.; Veroustraete, F. Comparison and Conversion of AVHRR GIMMS and SPOT VEGETATION NDVI Data in China. *Int. J. Remote Sens.* **2010**, *31*, 2377–2392. [[CrossRef](#)]
42. Tarnavsky, E.; Garrigues, S.; Brown, M. Multiscale Geostatistical Analysis of AVHRR, SPOT-VGT, and MODIS Global NDVI Products. *Remote Sens. Environ.* **2008**, *112*, 535–549. [[CrossRef](#)]
43. Ni, Z.; Yang, Z.; Li, W.; Zhao, Y.; He, Z. Decreasing Trend of Geohazards Induced by the 2008 Wenchuan Earthquake Inferred from Time Series NDVI Data. *Remote Sens.* **2019**, *11*, 2192. [[CrossRef](#)]
44. Yunus, A.P.; Fan, X.; Tang, X.; Jie, D.; Xu, Q.; Huang, R. Decadal Vegetation Succession from MODIS Reveals the Spatio-Temporal Evolution of Post-Seismic Landsliding after the 2008 Wenchuan Earthquake. *Remote Sens. Environ.* **2020**, *236*, 111476. [[CrossRef](#)]
45. Zhang, W.; Lin, J.; Peng, J.; Lu, Q. Estimating Wenchuan Earthquake Induced Landslides Based on Remote Sensing. *Int. J. Remote Sens.* **2010**, *31*, 3495–3508. [[CrossRef](#)]
46. Liu, X. Vegetation Indices Based on Different Sources of Remote Sensing Data Analyzed in Qinling Region. Master's Thesis, Chang'an University, Xi'an, China, 2015.
47. An, Y.; Gao, W.; Gao, Z.; Liu, C.; Shi, R. Trend Analysis for Evaluating the Consistency of Terra MODIS and SPOT VGT NDVI Time Series Products in China. *Front. Earth Sci.* **2015**, *9*, 125–136. [[CrossRef](#)]
48. Chen, J.; Jönsson, P.; Tamura, M.; Gu, Z.; Matsushita, B.; Eklundh, L. A Simple Method for Reconstructing a High-Quality NDVI Time-Series Data Set Based on the Savitzky–Golay Filter. *Remote Sens. Environ.* **2004**, *91*, 332–344. [[CrossRef](#)]
49. Savitzky, A.; Golay, M.J.E. Smoothing and Differentiation of Data by Simplified Least Squares Procedures. *Anal. Chem.* **1964**, *36*, 1627–1639. [[CrossRef](#)]
50. Beck, P.S.A.; Atzberger, C.; Høgda, K.A.; Johansen, B.; Skidmore, A.K. Improved Monitoring of Vegetation Dynamics at Very High Latitudes: A New Method Using MODIS NDVI. *Remote Sens. Environ.* **2006**, *100*, 321–334. [[CrossRef](#)]
51. Roerink, G.J.; Menenti, M.; Verhoef, W. Reconstructing Cloudfree NDVI Composites Using Fourier Analysis of Time Series. *Int. J. Remote Sens.* **2000**, *21*, 1911–1917. [[CrossRef](#)]
52. Das, M.; Ghosh, S.K. A Deep-Learning-Based Forecasting Ensemble to Predict Missing Data for Remote Sensing Analysis. *IEEE J. Sel. Top. Appl. Earth Obs. Remote Sens.* **2017**, *10*, 5228–5236. [[CrossRef](#)]
53. Dardel, C.; Kergoat, L.; Hiernaux, P.; Mougin, E.; Manuela, G.; Tucker, C. Re-Greening Sahel: 30 Years of Remote Sensing Data and Field Observations (Mali, Niger). *Remote Sens. Environ.* **2014**, *140*, 350–364. [[CrossRef](#)]

54. Van Leeuwen, W.; Orr, B.J.; Marsh, S.; Herrmann, S. Multi-Sensor NDVI Data Continuity: Uncertainties and Implications for Vegetation Monitoring Applications. *Remote Sens. Environ.* **2006**, *100*, 67–81. [[CrossRef](#)]
55. Wang, L.; Qu, J.J.; Xiong, X.; Hao, X.; Xie, Y.; Che, N. A New Method for Retrieving Band 6 of Aqua MODIS. *IEEE Geosci. Remote Sens. Lett.* **2006**, *3*, 267–270. [[CrossRef](#)]
56. Boyte, S.P.; Wylie, B.K.; Rigge, M.B.; Dahal, D. Fusing MODIS with Landsat 8 Data to Downscale Weekly Normalized Difference Vegetation Index Estimates for Central Great Basin Rangelands, USA. *GIScience Remote Sens.* **2018**, *55*, 376–399. [[CrossRef](#)]
57. Wei, J.; Wang, L.; Liu, P.; Chen, X.; Li, W.; Zomaya, A.Y. Spatiotemporal Fusion of MODIS and Landsat-7 Reflectance Images via Compressed Sensing. *IEEE Trans. Geosci. Remote Sens.* **2017**, *55*, 7126–7139. [[CrossRef](#)]
58. Shen, H.; Li, X.; Cheng, Q.; Zeng, C.; Yang, G.; Li, H.; Zhang, L. Missing Information Reconstruction of Remote Sensing Data: A Technical Review. *IEEE Geosci. Remote Sens. Mag.* **2015**, *3*, 61–85. [[CrossRef](#)]
59. Li, S.; Xu, L.; Jing, Y.; Yin, H.; Li, X.; Guan, X. High-Quality Vegetation Index Product Generation: A Review of NDVI Time Series Reconstruction Techniques. *Int. J. Appl. Earth Obs. Geoinf.* **2021**, *105*, 102640. [[CrossRef](#)]
60. Zhang, Q.; Yuan, Q.; Zeng, C.; Li, X.; Wei, Y. Missing Data Reconstruction in Remote Sensing Image with a Unified Spatial–Temporal–Spectral Deep Convolutional Neural Network. *IEEE Trans. Geosci. Remote Sens.* **2018**, *56*, 4274–4288. [[CrossRef](#)]
61. Zhang, Q.; Yuan, Q.; Li, J.; Li, Z.; Shen, H.; Zhang, L. Thick Cloud and Cloud Shadow Removal in Multitemporal Imagery Using Progressively Spatio-Temporal Patch Group Deep Learning. *ISPRS J. Photogramm. Remote Sens.* **2020**, *162*, 148–160. [[CrossRef](#)]
62. Xu, T.; Wang, Y.; Fu, B. Evaluation on sensibility of soil erosion of harder-hit area of Wenchuan Earthquake. *Soil Water Conserv. China* **2011**, *1*, 39–42+67. [[CrossRef](#)]
63. Wolters, E.; Dierckx, W.; Iordache, M.-D.; Swinnen, E. PROBA-V Products User Manual v3.01. 2018.
64. Jiao, Q.; Liu, L.; Li, Z.; Yue, Y.; Hu, Y. Assessment of Spatio-Temporal Variations in Vegetation Recovery after the Wenchuan Earthquake Using Landsat Data. *Nat. Hazards* **2014**, *70*, 1309–1326. [[CrossRef](#)]
65. Yu, S.; Liu, J.; Yuan, J. Vegetation Change of Yamzho Yumco Basin in Southern Tibet Based on SPOT-VGT NDVI. *Spectrosc. Spectr. Anal.* **2010**, *30*, 1570–1574. [[CrossRef](#)]
66. Sun, J. 1982~2000 Vegetation Change in China and Response of Typical Areas with Climatic Factors. Master’s Thesis, Nanjing University of Information Science & Technology, Nanjing, China, 2007.
67. Yuan, Q.; Shen, H.; Li, T.; Li, Z.; Li, S.; Jiang, Y.; Xu, H.; Tan, W.; Yang, Q.; Wang, J.; et al. Deep Learning in Environmental Remote Sensing: Achievements and Challenges. *Remote Sens. Environ.* **2020**, *241*, 111716. [[CrossRef](#)]
68. Muhammad, K.; Ahmad, J.; Baik, S.W. Early Fire Detection Using Convolutional Neural Networks during Surveillance for Effective Disaster Management. *Neurocomputing* **2018**, *288*, 30–42. [[CrossRef](#)]
69. Huang, B.; Zhao, B.; Song, Y. Urban Land-Use Mapping Using a Deep Convolutional Neural Network with High Spatial Resolution Multispectral Remote Sensing Imagery. *Remote Sens. Environ.* **2018**, *214*, 73–86. [[CrossRef](#)]
70. Shimobaba, T.; Kakue, T.; Ito, T. Convolutional Neural Network-Based Regression for Depth Prediction in Digital Holography. In Proceedings of the 2018 IEEE 27th International Symposium on Industrial Electronics (ISIE), Cairns, Qld, Australia, 13–15 June 2018; pp. 1323–1326. [[CrossRef](#)]
71. Zhang, R.; Di, B.; Luo, Y.; Deng, X.; Grieneisen, M.L.; Wang, Z.; Yao, G.; Zhan, Y. A Nonparametric Approach to Filling Gaps in Satellite-Retrieved Aerosol Optical Depth for Estimating Ambient PM<sub>2.5</sub> Levels. *Environ. Pollut.* **2018**, *243*, 998–1007. [[CrossRef](#)]
72. Stow, D.; Daeschner, S.; Hope, A.; Douglas, D.; Petersen, A.; Myneni, R.; Zhou, L.; Oechel, W. Variability of the Seasonally Integrated Normalized Difference Vegetation Index Across the North Slope of Alaska in the 1990s. *Int. J. Remote Sens.* **2003**, *24*, 1111–1117. [[CrossRef](#)]
73. Gao, X.; Huete, A.R.; Ni, W.; Miura, T. Optical–Biophysical Relationships of Vegetation Spectra without Background Contamination. *Remote Sens. Environ.* **2000**, *74*, 609–620. [[CrossRef](#)]
74. Wan, X. Vegetation Restoration and Its Effects on Soil after Converting Agricultural Lands to Forest. Master’s Thesis, Sichuan Agricultural University, Yaan, China, 2003.
75. Xie, Y.; Shao, Z.; Lan, X.; Li, F.; Zeng, F. Relationship Between Land Use and Soil Erosion in Karst Area—A Case Study of Bijie Experimental Area. *Res. Soil Water Conserv.* **2017**, *24*, 1–5. [[CrossRef](#)]
76. Tian, F.; Fensholt, R.; Verbesselt, J.; Grogan, K.; Horion, S.; Wang, Y. Evaluating Temporal Consistency of Long-Term Global NDVI Datasets for Trend Analysis. *Remote Sens. Environ.* **2015**, *163*, 326–340. [[CrossRef](#)]
77. Hong, Y.; Zhao, Y.; Wang, Y.; Xin, C.; Zhao, Y. Temporal and Spatial Variation Characteristics of Vegetation Restoration Based on MODIS-NDVI Wenchuan Earthquake Region in Ten Years. *Sci. Technol. Eng.* **2019**, *19*, 64–74.
78. Li, J.; Cao, M.; Qiu, H.; Xue, B.; Hu, S.; Cui, P. Spatial-temporal process and characteristics of vegetation recovery after Wenchuan earthquake: A case study in Longxi River basin of Dujiangyan, China. *Chin. J. Appl. Ecol.* **2016**, *27*, 3479–3486. [[CrossRef](#)]
79. Chen, N.; Lu, Y.; Zhou, H.; Deng, M.; Han, D. Combined Impacts of Antecedent Earthquakes and Droughts on Disastrous Debris Flows. *J. Mt. Sci.* **2014**, *11*, 1507–1520. [[CrossRef](#)]
80. Di, B.; Zhang, H.; Liu, Y.; Li, J.; Chen, N.; Stamatopoulos, C.A.; Luo, Y.; Zhan, Y. Assessing Susceptibility of Debris Flow in Southwest China Using Gradient Boosting Machine. *Sci. Rep.* **2019**, *9*, 12532. [[CrossRef](#)]
81. Jiang, W.-G.; Jia, K.; Wu, J.-J.; Tang, Z.-H.; Wang, W.-J.; Liu, X.-F. Evaluating the Vegetation Recovery in the Damage Area of Wenchuan Earthquake Using MODIS Data. *Remote Sens.* **2015**, *7*, 8757–8778. [[CrossRef](#)]
82. Cui, P. *Atlas of Mountain Hazards and Soil Erosion in the Upper Yangtze*; Science Press: Beijing, China, 2014.

83. Xu, C. Detailed Inventory of Landslides Triggered by the 2008 Wenchuan Earthquake and Its Comparison with Other Earthquake Events in the World. *Sci. Technol. Rev.* **2012**, *30*, 18–26.
84. Liu, Y.; Liu, R.; Ge, Q. Evaluating the Vegetation Destruction and Recovery of Wenchuan Earthquake Using MODIS Data. *Nat. Hazards* **2010**, *54*, 851–862. [[CrossRef](#)]
85. Cui, P.; Lin, Y.; Chen, C. Destruction of Vegetation Due to Geo-Hazards and Its Environmental Impacts in the Wenchuan Earthquake Areas. *Ecol. Eng.* **2012**, *44*, 61–69. [[CrossRef](#)]
86. Yang, W.; Qi, W.; Zhou, J. Decreased Post-Seismic Landslides Linked to Vegetation Recovery after the 2008 Wenchuan Earthquake. *Ecol. Indic.* **2018**, *89*, 438–444. [[CrossRef](#)]
87. Chen, M.; Tang, C.; Xiong, J.; Shi, Q.Y.; Li, N.; Gong, L.F.; Wang, X.D.; Tie, Y. The Long-Term Evolution of Landslide Activity near the Epicentral Area of the 2008 Wenchuan Earthquake in China. *Geomorphology* **2020**, *367*, 107317. [[CrossRef](#)]
88. Zhong, C.; Li, C.; Gao, P.; Li, H. Discovering Vegetation Recovery and Landslide Activities in the Wenchuan Earthquake Area with Landsat Imagery. *Sensors* **2021**, *21*, 5243. [[CrossRef](#)] [[PubMed](#)]
89. Baldi, G.; Noretto, M.D.; Aragón, R.; Aversa, F.; Paruelo, J.M.; Jobbágy, E.G. Long-Term Satellite NDVI Data Sets: Evaluating Their Ability to Detect Ecosystem Functional Changes in South America. *Sensors* **2008**, *8*, 5397–5425. [[CrossRef](#)] [[PubMed](#)]
90. Shen, P.; Zhang, L.M.; Fan, R.L.; Zhu, H.; Zhang, S. Declining Geohazard Activity with Vegetation Recovery during First Ten Years after the 2008 Wenchuan Earthquake. *Geomorphology* **2020**, *352*, 106989. [[CrossRef](#)]
91. Hu, G.; Chen, N.; Tanoli, J.I.; Liu, M.; Liu, R.-K.; Chen, K.-T. Debris Flow Susceptibility Analysis Based on the Combined Impacts of Antecedent Earthquakes and Droughts: A Case Study for Cascade Hydropower Stations in the Upper Yangtze River, China. *J. Mt. Sci.* **2017**, *14*, 1712–1727. [[CrossRef](#)]

**Disclaimer/Publisher’s Note:** The statements, opinions and data contained in all publications are solely those of the individual author(s) and contributor(s) and not of MDPI and/or the editor(s). MDPI and/or the editor(s) disclaim responsibility for any injury to people or property resulting from any ideas, methods, instructions or products referred to in the content.